



POLYTECHNIC OF TURIN

Master Thesis in Biomedical Engineering

**Exploring in-stent hemodynamics after
abdominal aortic endovascular
interventions: a computational study**

Candidate:

Valeria MASCHIO

Supervisors:

Prof. Umberto MORBIDUCCI

Prof. Stéphane AVRIL

Co-Supervisor:

Prof. Diego GALLO

PhD. Sabrina BEN AHMED

Academic Year 2018-2019

Theory is when you know everything, but nothing works. Practice is when everything works but no one knows why. In our lab, theory and practice are combined: nothing works, and no one knows why.

Albert Einstein

To my parents...

Abstract

Endovascular Aneurysm Repair (EVAR) is an innovative technique for the treatment of abdominal aortic aneurysm (AAA).

However, complex anatomies, characterized by localized aneurysms close to the renal arteries and vessel tortuosity, lead to post-operative complications. To help prevent them, a computational study explores hemodynamics within the stents.

The aim of this work is to compare the hemodynamic impact of different endoprosthesis in a male 68 years old patient having a short aortic neck and a fenestrated stent (f-EVAR) implant, which experienced an iliac arteries rotation after surgery.

Patient-specific CAD models of the aorta, before the intervention and after the f-EVAR implant, are built using a manual segmentation by the CT-scans.

Computational fluid dynamics (CFD) simulations are performed using the finite-element code CRISMON setting the patient-specific inflow and the 3-elements Windkessel model at each outlet as boundary condition.

The chimneys stent (Ch-EVAR) model, instead, is built by simulating the stent-graft model deployment inside the tortuous arterial model generated from patient pre-operative scan using Abaqus software.

CFD, in fact, requires an input from the finite element (FE) simulation to obtain a reliable and precise fluid domain (the stent-graft implant surface).

A second f-EVAR model is built without evaluate the iliacs rotation for a better hemodynamic comparison. On the stent main-body of the Ch-EVAR, the chimneys have been replaced by the fenestrated arteries.

The technique used to build the Ch-EVAR model simulating the deployment of the stent from the pre-operative scan cannot, indeed, predict the rotation of the iliac arteries.

CFD simulation of the preoperative, fenestrated and chimneys models is performed to analysed and compared hemodynamic aspects.

Looking at the blood flow, blood pressure and Wall Shear Stress (WSS) for the EVAR models, the postoperative hemodynamic changes that affect the preoperative hemodynamic are analyzed, focus on the renal arteries.

The alteration and higher complexity of postoperative geometry compared to the physiological one leads to an increase in pressure in the renal arteries, that is associated to the risk of complications such as stent migration and endoleaks.

The presence of recirculation flow in the stent midsections and of low WSS areas immediately after the stent could lead to aortic remodeling and thrombus formation respectively.

Although the WSS distribution areas are similar for fenestrated models, the model with iliac rotation is characterized by much different pressure and velocity values from those of the preoperative model, compared to the ch-EVAR and simulated fenestrated model.

Indeed, although some hemodynamic features in the simulated chimney model without iliac rotation and the patient-specific fenestrated model are comparable, it would be necessary to find a method to also predict the correct deployment of the iliac arteries from the preoperative CT-scan.

Despite the findings, all procedures must be evaluated individually, based on the severity of the injury, on the patient anatomy and evaluating the risk / benefit ratio of the intervention.

List of Abbreviations

AAA Abdominal Aortic Aneurysm

CAD Computer aided design

CFD Computational Fluid Dynamics

CG Chimney Graft

E Young Modulus

EVAR Endovascular Aneurysm Repair

FE Finite Element

FEM Finite Element Method

SG Stent Graft

Ch-EVAR Chimney endovascular aneurysm repair

CSG Chimney Stent Graft

f-EVAR Fenestrated endovascular aneurysm repair

BC Boundary Condition

OSR Open surgery repair

ECM Extra cellular matrix

NIH Neointimal hyperplasia

WSS Wall shear stress

TAWSS Time average wall shear stress

CT Computed Tomography

CVD Cardiovascular diseases

PreOP Preoperative model

PostOP postoperative model

Rp Proximal Resistance

Rd Distal Resistance

C Compliance

RCRs Proximal Resistance Capacitance Distal Resistance

RRA Right Renal Artery

LRA Left Renal Artery

RIA Right Iliac Artery

LIA Left Iliac Artery

PET Polyethylene terephthalate

PTF Polytetrafluoro

Contents

1	INTRODUCTION	12
2	BACKGROUND	13
2.1	Anatomy of the Aorta	13
2.2	Abdominal aortic aneurysm	14
2.3	Medical Imaging Modalities	15
2.4	Medical treatments options	16
2.4.1	Open Surgical Repair (OSR)	17
2.4.2	Endovascular Aneurysm Repair (EVAR)	17
2.5	Complications due to endoprosthesis interventions	19
2.6	EVAR and the effects on the renal arteries	21
3	MATERIALS AND METHODS	24
3.1	3D preoperative and f-EVAR patient-specific model building	25
3.2	Governing Equations and Flow properties	27
3.3	Wall properties	29
3.4	Mesh	29
3.5	Boundary conditions	30
3.6	Ch-EVAR model building	33
3.6.1	Preoperative model	34
3.6.2	Morphing	36
3.6.3	Guide wires deployment	39
3.6.4	SG main body, limbs and chimneys modeling	39
3.6.5	SG crimping	41
3.6.6	Stent placement and deployment	43
3.7	f-EVAR model without iliac arteries rotation	46
3.8	Solver parameters	47
3.9	Post-processing	47
3.10	Patient	48
4	RESULTS	51

4.1	Hemodynamic in the global model	51
4.1.1	Pressure waveform analysis	51
4.1.2	Flow waveform analysis	54
4.2	Hemodynamic in the renal arteries	55
4.2.1	Velocity stream-lines distribution	55
4.2.2	Proximal part of the stent	58
4.2.3	Stent midsection	59
4.2.4	Distal part of the stent	62
4.2.5	After the stent	64
4.3	Wall shear stress analysis	65
4.4	Evaluation of renal arteries angulation before and after stent implant	69
	5 DISCUSSION	71
5.1	State of the art and achievements	71
5.2	Limitations and future development	74
	6 CONCLUSION	75
	7 REFERENCES	77

1 Introduction

Endovascular Aneurysm Repair (EVAR) is a very low-invasive technique, alternative to Open Surgical Repair (OSR), which reduces the recovery time following the treatment of abdominal aortic aneurysm (AAA).

To avoid the limits due to complex vascular anatomies, fenestrated (f-EVAR) and chimneys (ch-EVAR) stent-grafts were developed.

The SG consists of a custom proximal main body and a bifurcated distal part in which the components of the iliac limb are embedded.

The f-EVAR main-body has fenestrations to preserve the flow in the renal arteries, instead Ch-EVAR main-body has in parallel two tubular covered stents (chimneys).

The SG implant excludes the vessel wall, already thinned by the aneurysm, from the pulsatile blood pressure.

However, these devices are characterized by post-operative complications due to stent migration or endoleaks, among the most common.

To avoid them, the proximal part of the stent is anchored close to the renal arteries and uncovered, so consisting only in a metal hold that could compromise the vessels.

Besides, the devices alter the native anatomy and so the hemodynamic changes.

The CFD, in this sense, is used in the vascular devices design and evaluation, to plan vascular interventions and to prevent post-operative complications that could limit the EVAR technique use.

The purpose of present activity is to compare the hemodynamic in f-EVAR and Ch-EVAR stents in a 68-year-old male patient having a juxta-renal abdominal aortic aneurysm treated by an f-EVAR implant.

2 Background

2.1 Anatomy of the Aorta

The aorta is the largest and the most important artery in the human body; it transports the oxygenated blood from the heart to peripheral vascular system (1). The human aorta is divided into thoracic aorta and abdominal aorta. The thoracic aorta starts from the heart and ends in the diaphragm, while the abdominal aorta takes place from the abdominal region and extends until the aortic bifurcation.

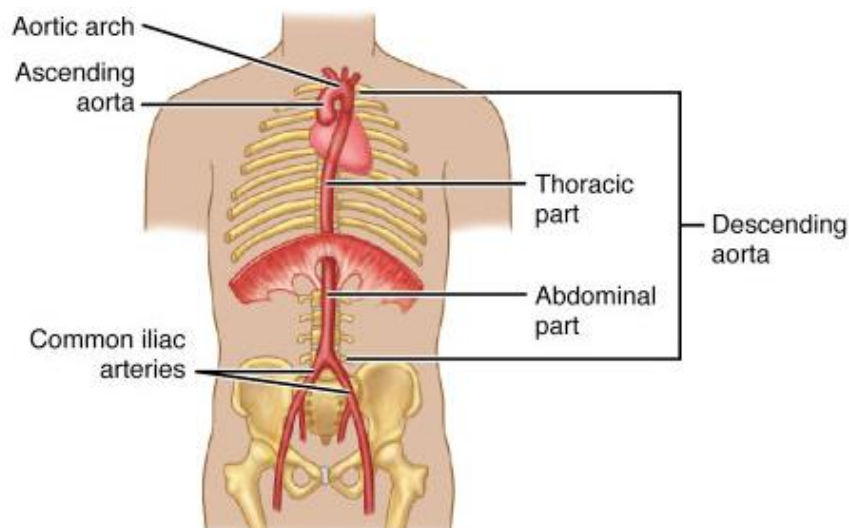


Figure 2.1: Aorta Diramation. Reprinted by (2)

“Like all arteries, aorta's wall has 3 layers:

- Intima, the innermost layer, provides a smooth surface for blood to flow across.
- Media, the middle layer with muscle and elastic fibers, allows the aorta to expand and contract with each heartbeat.

- Adventitia, the outer layer, provides additional support and structure to the aorta” (3).

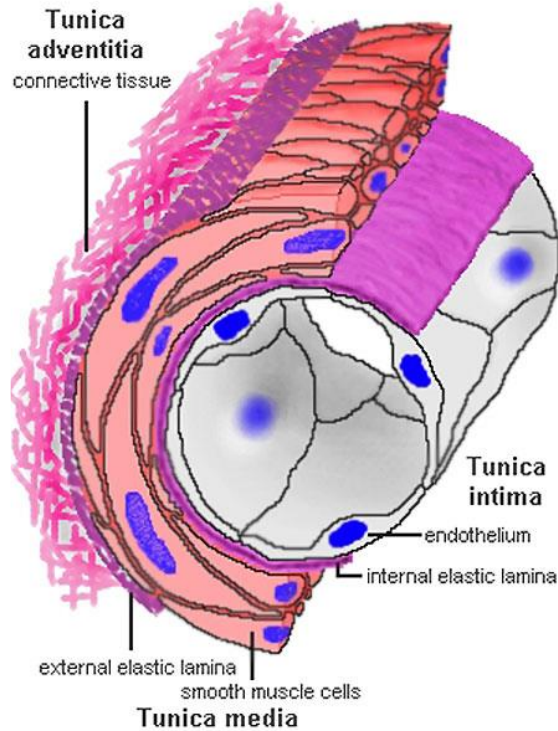


Figure 2.2: Three layers in the vessel wall. Reprinted by (4)

According to the vascular remodeling theory: structural changes such as the increase in the content of collagen and calcium deposits induce loss of compliance and an increase of the wall stiffness (5).

“These effects (elastin loss, axial stretch decrease) are expected to be more pronounced in the areas exposed to larger hemodynamic loading which would be more favorable to fatigue damage of elastin and aorta remodeling” (6).

2.2 Abdominal aortic aneurysm

When the aortic wall tissue weakness, following a cell degeneration, exceeding 50% of the initial diameter is called aneurysm (7).

The permanent deformation is related to the interaction between the “degenerative biological process and specific hemodynamic factors” (8), which lead to a change in the wall mechanical properties.

“It is appropriate to focus on the abdominal aorta, as 80% of all aortic aneurysms occur in the abdominal aorta in the infrarenal location” (9), just below the renal arteries, Figure 2.3, but above the point in which the descending aorta bifurcates into the two common iliac arteries (7).

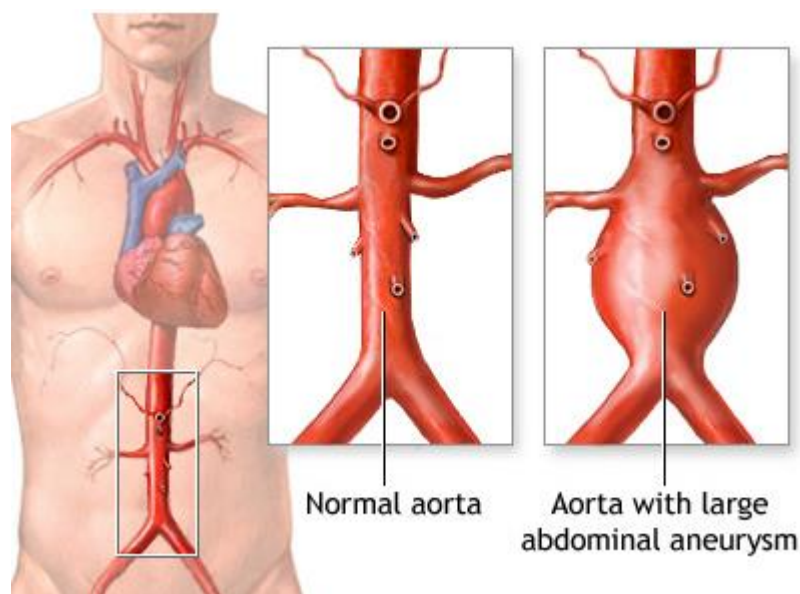


Figure 2.3: Abdominal aneurysm. Reprinted by (10)

According to epidemiological studies, AAAs are more common in older men than in women and young people. Furthermore, “the aneurysm rupture occurs in 1-3% of men aged 65 or more, the mortality is 70-95%” (7).

Triggering factors are related to lifestyle or diseases such as hypertension.

It is also noted that ethnicity influences the occurrence of the aneurysm. In the United Kingdom the rate of AAA in Caucasian men older than 65 years is about 4.7% while in Asian men it is 0.45% (11).

2.3 Medical Imaging Modalities

Recent advances in medical imaging techniques have assessed the use of 3D patient-specific geometries and computational meshes in the development of

Computational Fluid Dynamics (CFD) models. The main advantage of the use of these techniques is to provide accurate information about the anatomic characterization of the domain of interest.

Computed Tomography (CT) is an imaging modality mostly used for diseases diagnosis, treatment planning and research studies.

“It uses ionizing radiation (x-ray) and a contrast agent to identify the vessel lumen amongst the surrounding tissues.

Different tissues are distinguished based on their capability to absorb x-rays; moreover, the contrast agent allows highlighting the vascular lumen and facilitating the segmentation of the flow channel” (12). The main advantages of this technique are the high contrast-to-noise ratio, the high temporal resolution and the high spatial resolution. The principal disadvantage of this technique is the high quantity of ionizing radiation necessary to obtain images with high resolution.

A Doppler ultrasound, used to estimate the patient-specific inflow and mean flow at each arteries outlet, “is a noninvasive test that can be used to estimate the blood flow through blood vessels by bouncing high-frequency sound waves (ultrasound) off circulating red blood cells” (13).

2.4 Medical treatments options

Treatment options for AAA are conservative surveillance of the size and possibly surgery if the diameter increases and the associated pharmacological therapies fail to control the phenomenon.

In the case of a real rupture risk of the aneurysm, this can be prevented by open surgical repair (OSR) or endovascular aneurysm repair (EVAR) respectively, as shown in Figure 2.4. An intervention is often recommended if the aneurysm grows more than 1 cm per year or it is bigger than 5.5 cm (14).

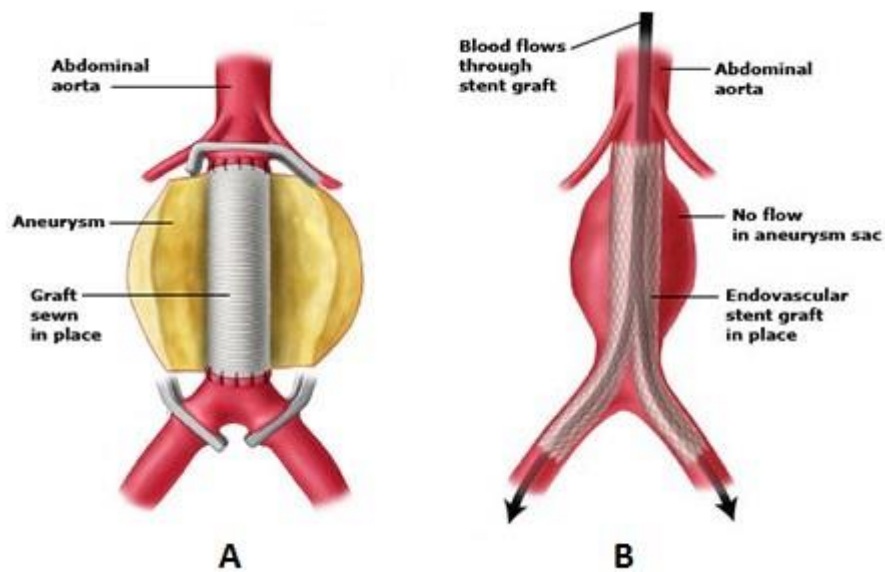


Figure 2.4: Aneurysm repair options. (a) Open surgical repair (OSR); (b) endovascular aneurysm repair (EVAR). Adapted from (15)

2.4.1 Open Surgical Repair (OSR)

The OSR is a technique that since 1951 is still used for patients at high risk of rupture, despite being highly invasive (7).

In fact, it consists in an abdominal incision to export the thrombus and replacing the weakened wall with a prosthetic graft.

The OSR “is associated with longer hospital stays, higher transfusion rates, greater use of intensive care resources, and higher 30-day mortality rates” (15).

2.4.2 Endovascular Aneurysm Repair (EVAR)

Endovascular surgery, whose first use dates back to 1991 (16), consists in excluding the aneurysm with a SG using the femoral arteries as entry points and a minimally invasiveness.

“The device (Fig. 2.5) is composed of a metallic main body (stainless steel or nitinol) covered by a fabric (polytetrafluoroethylene or polyester). It is placed against the aortic wall, thanks to the radial force of the stent-graft, in order to exclude the aneurysm from the systemic circulation” (17).

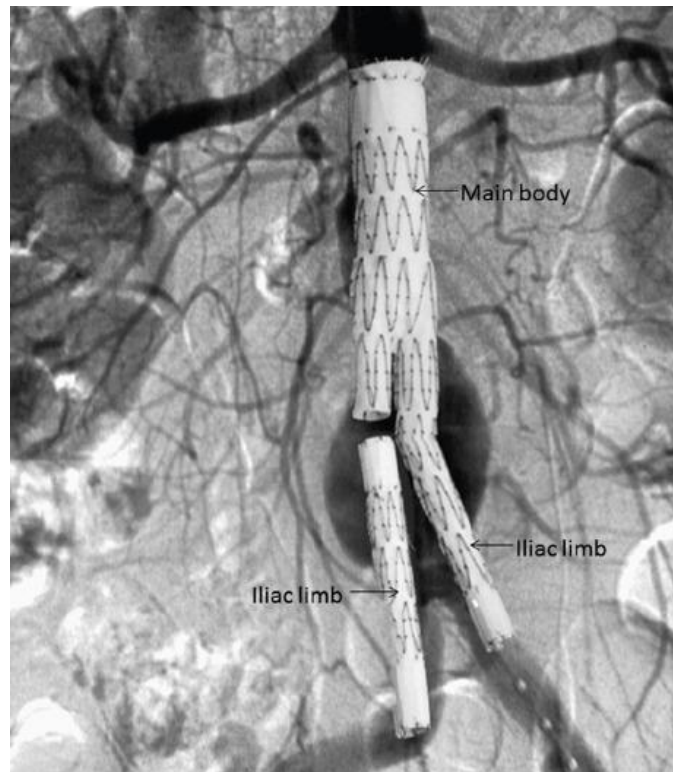


Figure 2.5: Components of a bifurcated aortic stent-graft. Reprinted by (17)

“It is estimated that 50% of patients with abdominal aortic aneurysms are not candidates for endovascular repair using the currently commercially available devices because of unfavorable anatomy” (18). The clinical failure includes patients with short infrarenal neck (<10-15 mm in length and > 32 mm in diameter (19)) or angulated (> 45° (20)) and complex aneurysmal involvement of the juxta-renal aorta.

To avoid these limits, new devices (Fig. 2.6) with fenestrated (f-EVAR) stents are developed, in order to “extend the proximal sealing zone and circumventing the limitation of short or absent aortic necks” (18).

They allow “incorporation of aortic side branches and preservation of end-organ perfusion while achieving aneurysm exclusion with a total endovascular approach” (21).

“Fenestrations imply side holes in the fabric of the stent-graft. These are reinforced by a nitinol ring to facilitate catheterization, prevent fraying of the fabric, and allow attachment of a side branch alignment stent” (21).

f-EVAR reduce perioperative morbidity (that is, the condition of being diseased during or around the time of an operation), mortality, hospital stay and recovery time, but a high degree of customization and long manufacturing time is required (21).

In case of emergency it isn't possible to wait for the manufactured time, therefore a new EVAR technique is developed, called “chimney”. This device (Fig. 2.7) has two tubular covered stents in parallel with the main one in order to maintain the renal arteries flow, would otherwise be blocked by the main aortic SG (22).

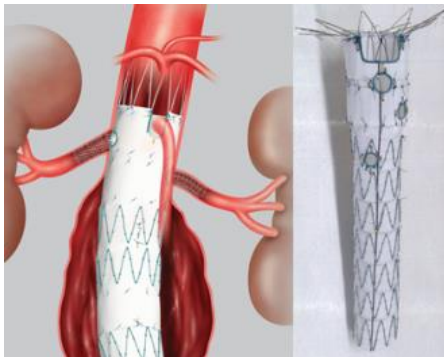


Figure 2.6: f-EVAR (7)

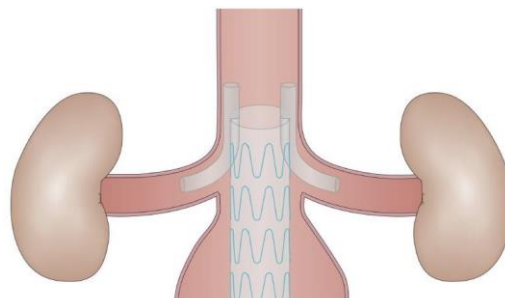


Figure 2.7: Ch-EVAR (7)

2.5 Complications due to endoprosthesis interventions

Possible problems that may develop during, or after, the endoprosthesis interventions are mainly due to three factors: operator dependent errors, patient's anatomy and factors related to the prosthesis itself (23).

These complications often require secondary surgery, which is one of the greatest challenges to the EVAR success.

The most frequent complications are:

- Prosthesis migration

The migration consists in a SG displacement of at least 5 mm from the area of the first location. This complication requires the necessity for a second patient intervention (23).

- Separation between the SG components

The separation between the various components of the prosthesis leads to the formation of an endoleak, a "leak" in the aneurysmal sac which would make it at high risk of rupture again. The cause is usually due to a new excessive pressure on the prosthesis (23).

- Occlusion or stenosis

This problem can be caused by a previously existing stenosis. It already appears after the first three months of surgery. The new generation SGs, more flexible, have reduced the number of cases (23).

- The endoleak (Fig. 2.8)

"Endoleak is the most common complication associated with the endovascular repair, defined as persistent blood flow in the aneurysm sac" (7).

It could "cause elevated intrasac pressure and high stresses in the abdominal aortic aneurysm wall causing AAA rupture and hence the need for a second procedure. Currently, five endoleak types are defined in the literature on the basis of the source of the leakage and usually named numerically: leakage at the anchor sites (Type I, if proximal Ia, if distal Ib), leakage via collateral

arteries (Type II), defective SG (Type III) and leakage owing to porosity of the graft material (Type IV) and endotension (Type V)” (7).

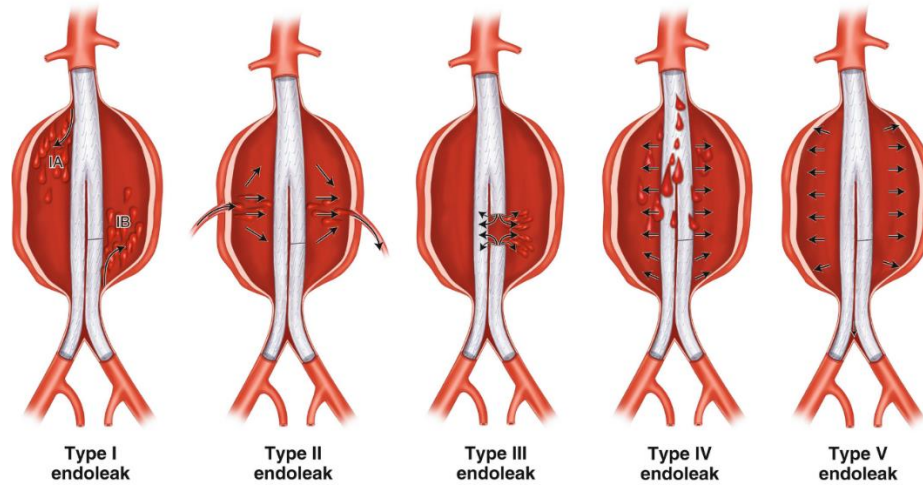


Figure 2.8: Endoleak Types. Reprinted by (24)

2.6 EVAR and the effects on the renal arteries

To solve the limits related to the use of EVAR, the SG is placed near the renal arteries in order to obtain a good seal around the upper neck of the aneurysm. Furthermore, an uncovered stent in the proximal part is preferred to limit migration.

However, despite a strong research into the used materials, usually nitinol or stainless steel covered with polyester or PTF (Polytetrafluoroethylene), there is the possibility that these may compromise the vessels (25).

The denuded artery wall and the stent struts, in fact, be highly thrombogenic surfaces. Not only the platelet aggregation but also the friction, due to the blood flow against the wall that can cause local wall shear stress (WSS) areas and therefore disturbances in the flow and turbulence near the vessel wall, are related to the risk of thrombosis.

The WSS is, indeed, the tangent force to the lumen of the vessel that play an important role in the stent performance (26).

“Within the first few weeks of stent implantation, smooth muscle cells (SMCs) that normally reside in the middle and outer layers of the artery migrate toward the inner surface” (27).

Duraiswamy et al. show that endothelial cells subjected to low wall shear stress (WSS) increase their production of “extracellular matrix proteins, which can form a large portion of the volume of neointimal hyperplasia (NIH)” (27). In patients treated with stents the restenosis process is entirely attributable to neointimal growth, as mentioned the application of stents in small-size vessels is associated, for unclear causes, with an increased myocellular proliferation.

Two main factors can be used to explain the phenomenon:

- 1) the high barotrauma on the deep layers of the arterial wall resulting from the frequent use of oversized balloon according to the vessel diameter;
- 2) the excessive concentration of metal per unit in the vessel surface (28).

During an EVAR the angiographic study reveals, also, concurrent vascular diseases. Some studies reported the presence of a stenosis of more than 50% in 20-40% of the renal arteries. Other authors have, instead, documented a “progression of a pre-existing renal arteriopathy” (29).

Through the biology mediated by endothelial cells, the WSS regulates the vascular remodeling.

The stress induced in the wall by the pressure is, indeed, felt by the cells of the vascular wall, that change the sense in the bloodstream and “transduce these mechanical signals into biological signals, activating pathways to maintain vascular homeostasis” (30).

The remodeling of the arterial wall plays a key role in the hypertension because it is associated with an increase in peripheral resistance and a reduction in vascular compliance, especially in small-diameter vessels.

Despite the findings, all procedures must be evaluated individually, based on the severity of the injury and the presumed risk of progression, evaluating the risk / benefit ratio of the intervention.

Chapter 3

3 Materials and methods

The aim of this work is to compare the hemodynamics in fenestrated (f-EVAR) and chimney (Ch-EVAR) stents in a male 68 years old patient having a localized aneurysm close to the renal arteries and an f-EVAR implant, which was affected to a iliac arteries rotation after surgery.

Patient-specific CAD models of the aorta before the intervention (preOP) and after the f-EVAR implant are developed on the CRIMSON open source platform using the segmentation by the CT-scans. The Ch-EVAR model, instead, is built using an innovative methodology that simulates the chimneys deployment within the renal arteries on the ABAQUS software, that is suites for finite element analysis and computer-aided engineering.

CFD, in fact, allows to evaluate the hemodynamic in f-EVAR and ch-EVAR to avoid postoperative complications, but requires an input from the finite element (FE) simulation to obtain a reliable and precise fluid domain (the SG implant surface).

A second f-EVAR model is built without evaluate the iliacs rotation for a better hemodynamic comparison. On the stent main-body of the Ch-EVAR, the chimneys have been replaced by the fenestrated arteries.

The technique used to build the Ch-EVAR model simulating the deployment of the stent from the pre-operative scan cannot, indeed, predict the rotation of the iliac arteries.

Looking at the blood flow, blood pressure and Wall Shear Stress for the three stent models, the postoperative hemodynamic changes that affect the preoperative hemodynamic are analyzed, focus in particular on the renal arteries.

To perform CFD, the CRIMSON software (31) is used on the École des mines de Saint-Étienne cluster.

CRIMSON is a finite element code software, specialized in cardiovascular simulations. It integrates the FSI (32) (Fluid Structure Interaction), a boundary conditions definition, medical image processing and mesh generating.

3.1 3D preoperative and f-EVAR patient-specific model building

Patient-specific models of the aorta before the surgery (preOP) and after the stent graft implantation (poOP), were built on the CRIMSON open source platform (Fig. 3.1).

Detailed anatomical imaging is required to create accurate 3D geometric models of the abdominal aorta in order to perform computational fluid dynamics (CFD) simulations. CT-scans were used to create the CAD model of the aorta by segmenting the imaging data. The differences in pixel intensity are used to detect vessel boundaries by manual interaction. Then, an automated lofting process interpolates all segmented contours and creates the 3D model of the aorta and its branches (33).

The fenestrated stent is integrated with the aorta using Boolean operations (Fig. 3.2, Fig. 3.3): the stent walls and the renal artery are considered as common, then the renal arteries are fused to the aorta and finally the stents are cut off from the aorta. The geometric model is used to create a detailed mesh of the aorta.

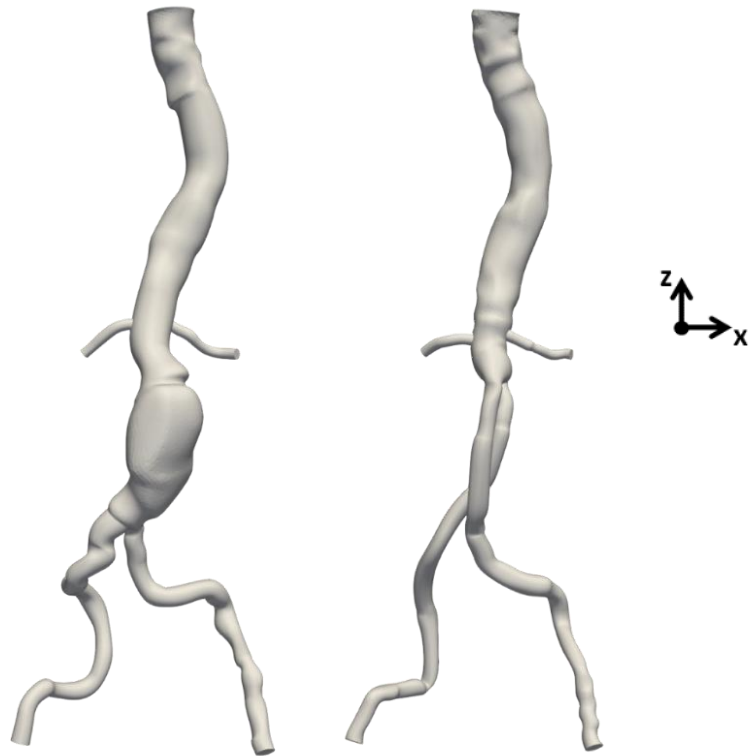


Figure 3.1: Patient-specific abdominal aorta pre-operative (PRE-op) and post-operative (f-Evar) models created with CRIMSON

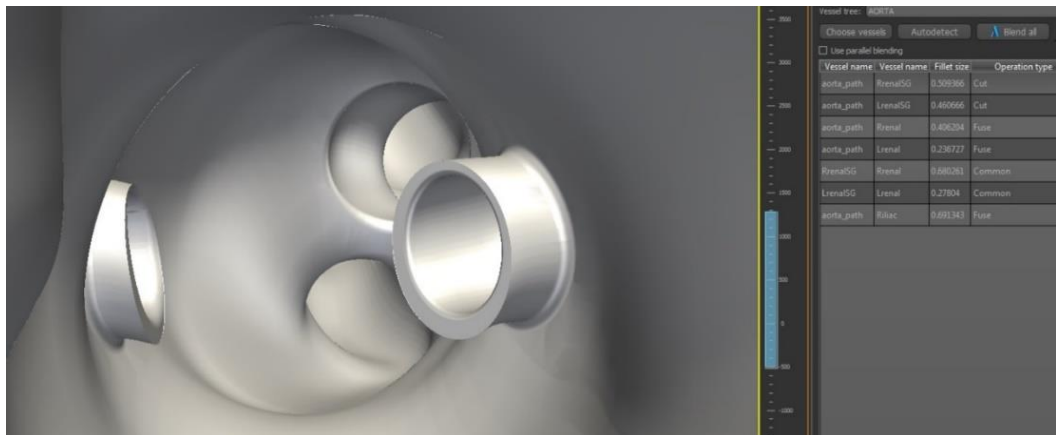


Figure 3.2: Boolean operations used (right side of the image) and a view of the interior of the aorta. In the foreground the protrusions of the stents and in the background the cavities of the two iliac arteries.

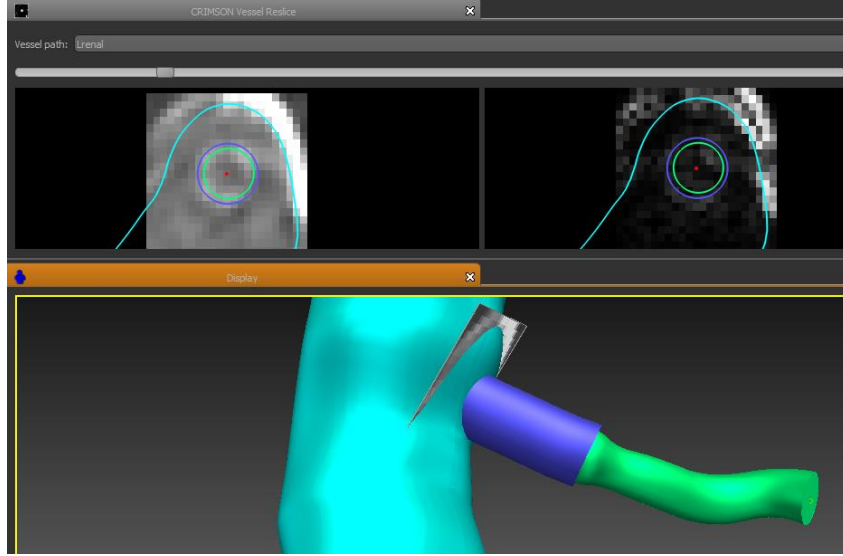


Figure 3.3: Stent manual segmentation. In turquoise the aorta, in blue the stent, in green the left renal artery and in red the center line projection.

3.2 Governing Equations and Flow properties

In this work the blood is considered as an incompressible fluid governed by the Navier-Stokes equations.

Mass (34) and momentum (35) conservation result in the following equations for a fluid element:

$$\nabla \cdot \vec{u} = 0 \quad (3.1)$$

$$\rho \frac{D\vec{u}}{Dt} = -\nabla \cdot \vec{\tau} - \nabla P \quad (3.2)$$

where \vec{u} is the velocity vector, ρ is the fluid density, $\vec{\tau}$ is the stress tensor and P is the pressure. The left side term of the equation 3.2 represents the convective forces; the first term on the right side is the stress viscous forces contribution and the other term represents the pressure forces acting on the fluid element.

The equation of mass conservation (3.1) is also called continuity equation and it “implies that an equal amount of mass that enters a volume also must leave it” (34). The equation of momentum conservation (3.2) means that the rate of change of momentum balances all the forces acting on the fluid element.

To close the system of equations is necessary to define the stress tensor $\vec{\tau}$, which depends on the fluid biomechanical properties (36).

Therefore, the equations 3.1 and 3.2 need to be solved together with an appropriate constitutive equation describing the fluid rheology.

The viscous fluid model used is the Newtonian fluid with density value of 0.00106 kg/m³ and a viscosity of 0.004 Pa.s (which is true for flows in large vessels (37)), based on the assumption that the stress tensor is directly proportional to the rate of deformation tensor (36).

The constitutive equation is usually expressed in the form:

$$\boldsymbol{\tau} = \mu \dot{\boldsymbol{\gamma}} \quad (3.3)$$

where μ is the viscosity and $\dot{\boldsymbol{\gamma}}$ is the deformation rate. In Newtonian fluids, the viscosity is independent from the variations in shear rate or shear stress. The relationship between shear rate and shear stress is represented by a slope which is constant over the range of shear stress examined, and thus the viscosity is constant, as shown in Figure 3.4.

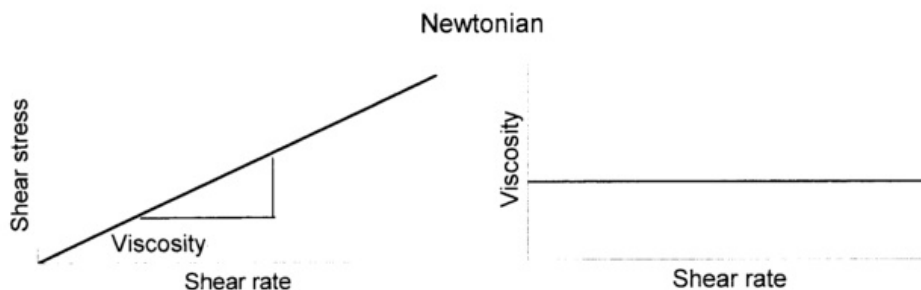


Figure 3.4: Shear stress-shear rate and viscosity-shear rate for Newtonian fluids. Adapted from (38).

3.3 Wall properties

An accurate model of the aortic wall should consider the nonlinearity and anisotropy of the wall, and the presence of three different layers with three different biomechanical properties. However, an estimation of in vivo patient-specific material properties is still a challenging problem (39) and the use of customized “computational models is being explored as a tool to improve clinical outcome. Including vessel wall motion in such simulations can provide more realistic and potentially accurate results, but requires significant additional computational resources, as well as expertise” (40). Because custom simulations should not be used as an intervention planning tool, then the additional complexity, experience, and computational expense required to model the movement of the wall is neglected.

The wall is considered as rigid and no-slip condition on the wall has been set.

3.4 Mesh

“Finite element tetrahedral meshes were iteratively refined until mesh-independent results were achieved” (41).

The table (Tab 3.1) shows an example of systolic pressure differences until reaching a mesh independence for the preOP model. The results are independent when these differences are less than 1%.

Table 3.1- Mesh adaptivities errors

	INLET	RRA	LRA	RIA	LIA
1st Mesh Adaptivity	1,97%	3,09%	3,99%	9,14%	7,36%
2st Mesh Adaptivity	1,89%	2,07%	2,24%	2,17%	2,59%
3st Mesh Adaptivity	0,70%	0,78%	0,74%	0,74%	0,99%
4st Mesh Adaptivity	0,15%	0,20%	0,33%	0,07%	0,23%

The elements were adapted according to velocity gradient residuals errors. A larger mesh (2 mm) is used at the level of the aorta and the iliac arteries, while a smaller mesh (between 0.1 mm and 0.2 mm) is used for renal arteries, where the most important speed is observed. For each model four mesh adaptations were necessary.

3.5 Boundary conditions

At the mesh nodes hemodynamic calculations can be made. In order to blood flow CFD simulations to be carried out, boundary conditions must be imposed at the inlet and at the outlets of the model. A key aspect in accurate CFD simulations is the specification of physiologically accurate boundary conditions (BCs) (33).

Patient-specific pulsatile blood flow from echocardiography is imposed at the inlet according to patient-specific systolic (128 mmHg) and diastolic pressure (80 mmHg) the initial pressure is set at 40 mmHg.

A 3-elements Windkessel (RCR) model (Fig. 3.5) is used to set BCs at the arteries outlets using simplified equations. It is an electric circuit analogue where the voltage difference is the drop-in arterial pressure and the electric current is the blood flow. Resistances (R) “represent arterial and peripheral resistance that occur as a result of viscous dissipation inside the vessels” (35), so the resistance that the blood finds flowing from the bigger to the smaller artery; the capacitor (C) represents “volume compliance of the vessels that allows them to store large amounts of blood” (35).

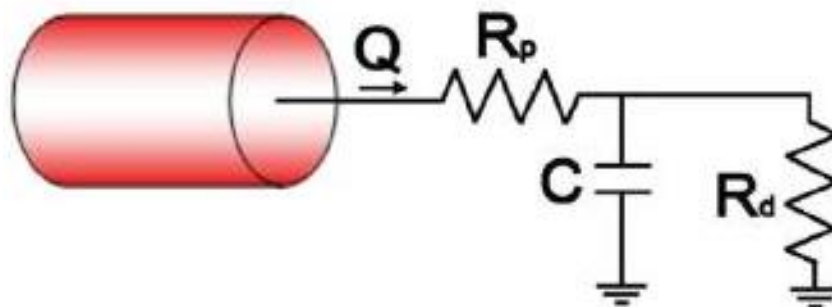


Figure 3.5: 3-elements Windkessel model. Reprinted by (42).

The parameters of the 3-element Windkessel model (proximal resistance (R_p), peripheral compliance (C) and distal resistance (R_d)) are obtained by a MATLAB code using 1D Nonlinear theory considerations and assuming minimization of wave-reflections at the outflow faces.

The model is set in CRIMSON (Fig. 3.6) imposing the found boundary conditions at each outlet (RCRs).

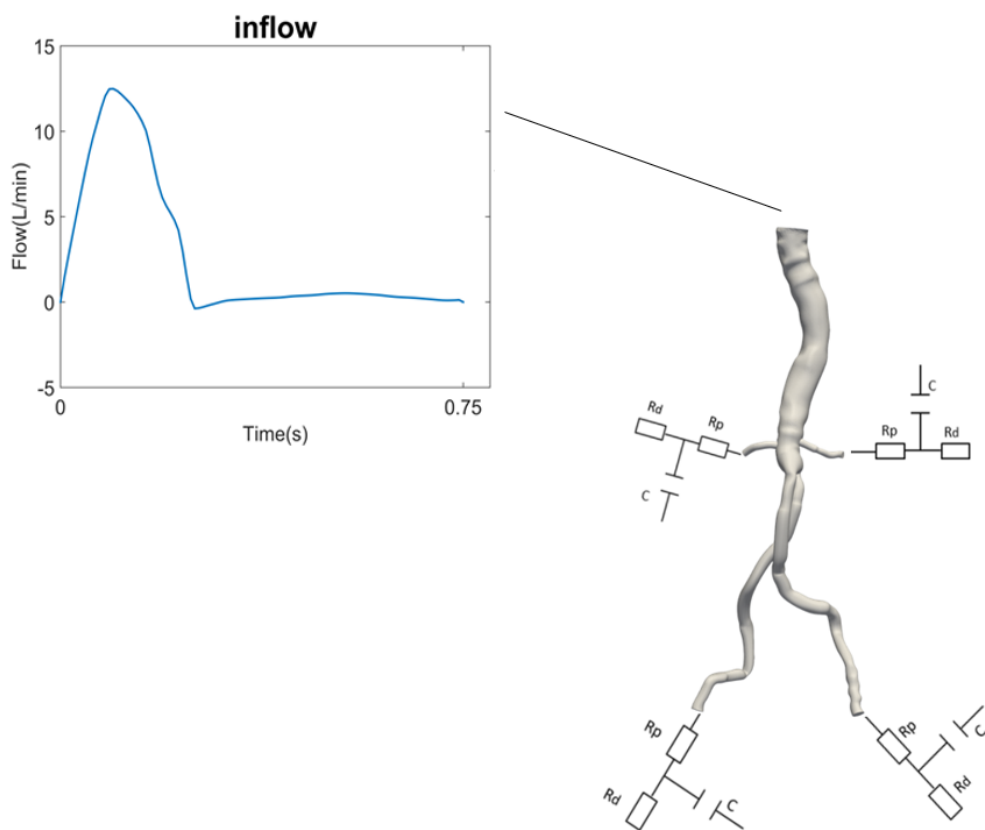


Figure 3.6: BCs of a patient-specific 3D aorta model created with CRIMSON.

Resistance Calculation

According to Ohm's law in a series circuit the total peripheral resistance (R_t) is:

$$R_T = \frac{P_{MEAN}}{Q_{MEAN}} \quad \frac{1}{R_T} = \sum_j \frac{1}{R^j} \quad (3.4)$$

It is possible to derive the distribution of total resistance (R^j) for each outlet j of the model using the relationship 3.5 and to split R^j into a proximal resistance R_1^j and a distal resistance R_2^j such the equation 3.6.

$$R^j = R_T \frac{Q_{MEAN}}{Q^j} \quad (3.5)$$

$$R^j = R_1^j + R_2^j \quad (3.6)$$

If stiffness and thickness are not known like in this case of rigid wall:

$$R_1^j = \frac{\rho c_{dias}^j}{A_{dias}^j} \quad c_{dias}^j = \frac{a_2}{(2R_{dias}^j)^{b_2}} \quad (3.7)$$

where c_{dias}^j is the diastolic wave speed at each outflow branches, A_{dias}^j is the diastolic area, R_{dias}^j is the diastolic radius of outlet j and a_2 and b_2 are two constants.

Compliance Calculation

The total compliance of the model is (C_T) is:

$$C_T = C_C + C_P \quad (3.8)$$

Where C_C is the “conduit compliance” in the 3D domain and C_P is the peripheral compliance assigned to the reduced-order models.

$$C_T = \frac{Q_{max} - Q_{min}}{P_{systolic} - P_{diastolic}} \Delta t_{Q_{min}^{Q_{max}}} \quad (3.9)$$

Where $\Delta t_{Q_{min}^{Q_{max}}}$ is the time from Q_{max} to Q_{min} and in a rigid model $C_C=0$.

$$C_P^j = C_P \frac{Q^j}{Q_{\text{mean}}} \left(\frac{R_1^j + R_2^j}{R_2^j} \right) \quad (3.10)$$

To find the BCs is possible to calculate Q^j , knowing the total area and the area at each outlet, using the ratio:

$$A_T = \sum_{i=1}^n A_{\text{dias}}^i \quad \frac{Q^j}{Q_{\text{mean}}} = \frac{A^j}{A_T} \quad (3.11)$$

RCRs optimizations

“The anatomical mesh and boundary conditions are then fed into a computational solver where blood flow simulations are carried out to solve a set of equations (e.g. Navier–Stokes equations for blood flow) enforcing conservation of mass (continuity). This calculates the relevant hemodynamic variables throughout the aorta which can then be post-processed to analyze for different flow characteristics and biomechanical forces” (33).

After two cardiac cycles mesh size and RCRs were tuned in order to obtain residuals $< 10^{-3}$ and simulated arteries blood flow split equal to the patient-specific flow split at each arterial outlet.

3.6 Ch-EVAR model building

EVAR involves high risk of secondary intervention to treat complications like endoleaks or thrombosis, especially in patients presenting challenging arterial anatomies. In this case, the aneurysm is located near the renal arteries so the CFD could be used to predict complications and adapt the type of complex EVAR to prevent them (43).

In order to have an accurate simulation of stent-graft (SG) deployed shape and to compare the renal arteries hemodynamics in f-EVAR and Ch-EVAR a SG model with chimneys is created using Abaqus software (Fig. 3.7).

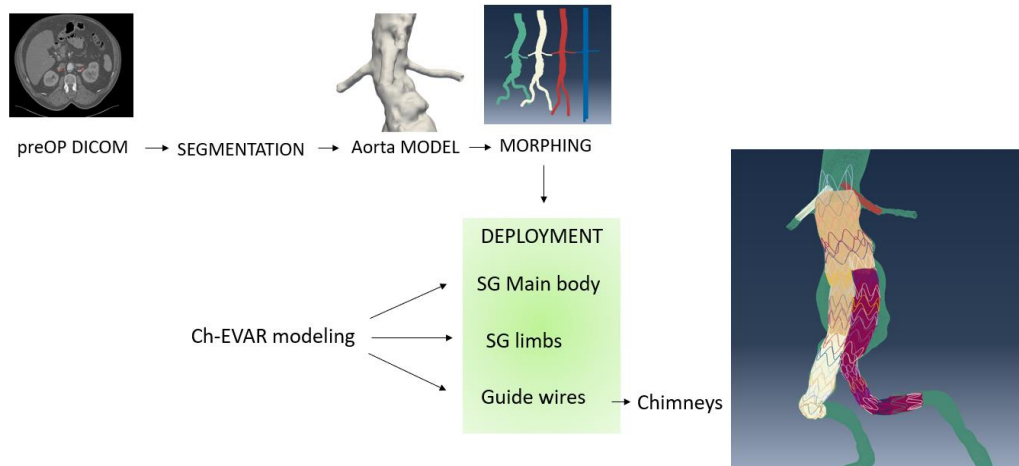


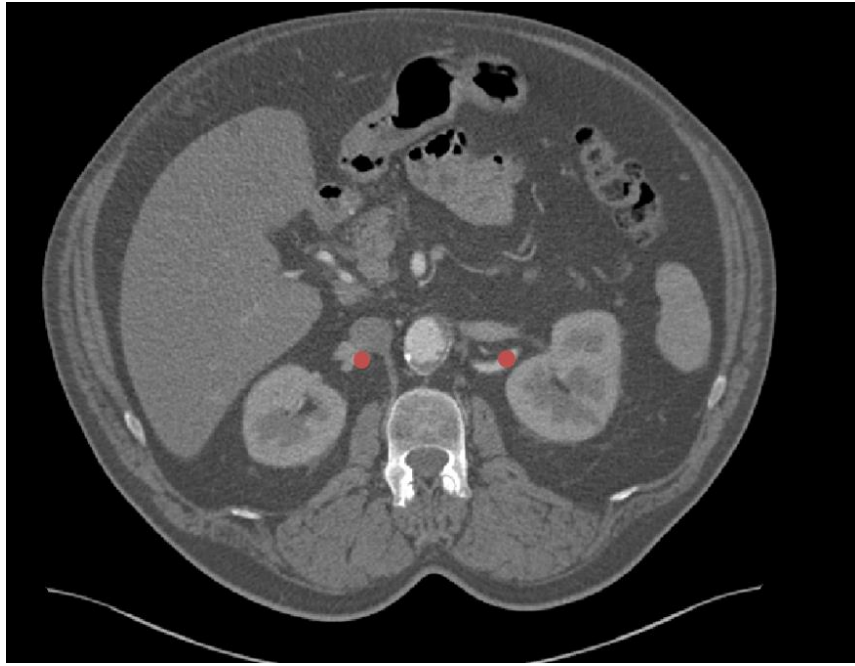
Figure 3.7 Ch-EVAR model building flowchart.

3.6.1 Preoperative model

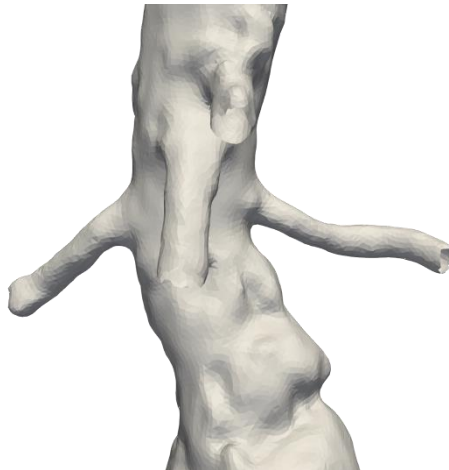
Preoperative model geometry and surface mesh are created from CT-scans through semi-automatic segmentation in VMTK.

Using the DICOM file and visualizing it, the ends of the arteries are identified by differences in pixel intensity and the preoperative model is generated (Fig. 3.8).

VMTK level set segmentation algorithm is run to obtain the volume of the arteries, from which the surface will be extracted. This surface is then meshed with 3-node triangle linear elements.



A

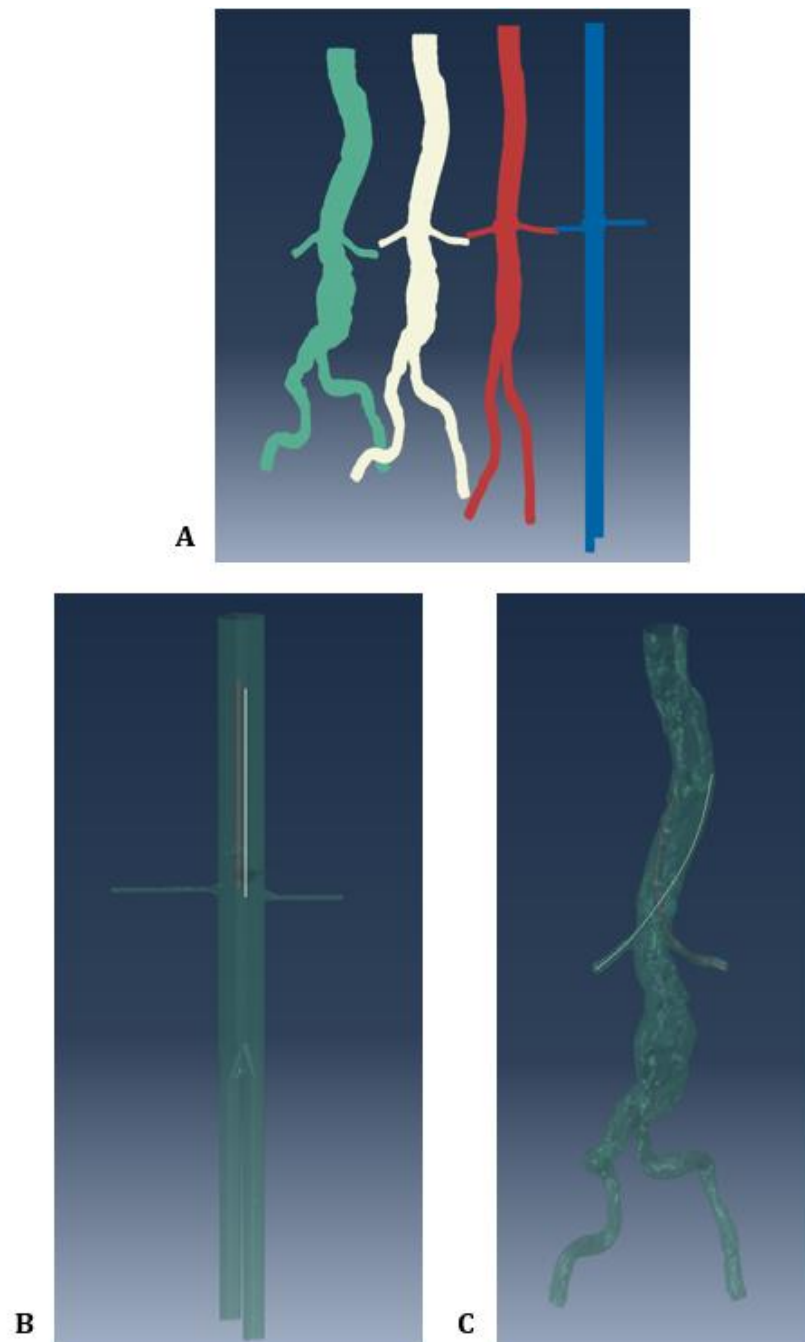


B

Figure 3.8: (A) Example of identification of the renal arteries extremities on the preOP CT-scan; (B) Generated arteries surface model. The two renal arteries generate by selecting the extremities with the red circles in the image on the left; the mesenteric and celiac arteries whose extremities were subsequently selected too.

3.6.2 Morphing

A Matlab code uses the previously generated data and input values to generate 3 different aorta shapes, up to the most cylindrical. This technique called “morphing” (Fig. 3.9-A) is used to arrive to an easy geometry, from the geometry of the patient to a more cylindrical one, where it will be easy to insert the guide wires or the stent-graft.



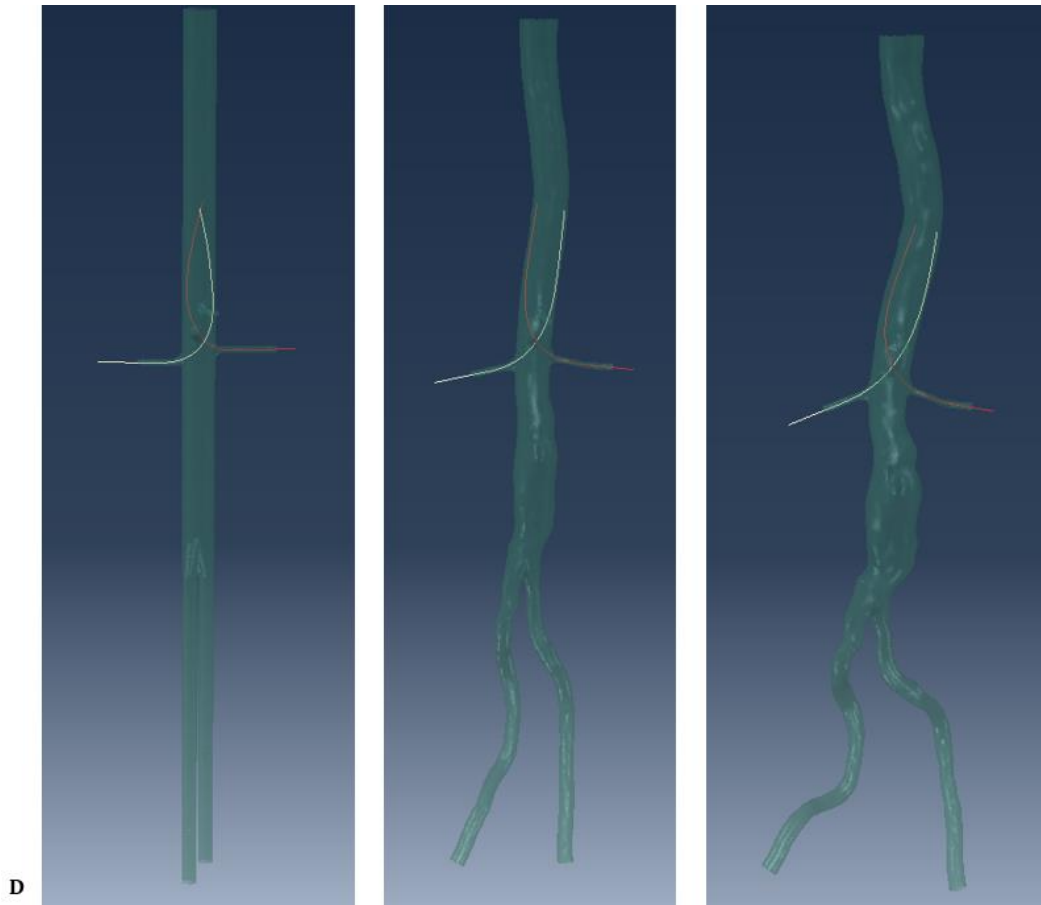


Figure 3.9: (A) Morphing technique. From left to right: the pre-OP patient-specific geometry and the simplified geometries up to the most cylindrical. (B) Aorta cylindrical geometry with the guide wires (red and white wires) aligned to the centerlines of the cylindrical arteries. (C) Guide wires deployment into the renal arteries of the preoperative model. (D) Intermediate steps between the cylindrical shape and the final shape of the preoperative model.

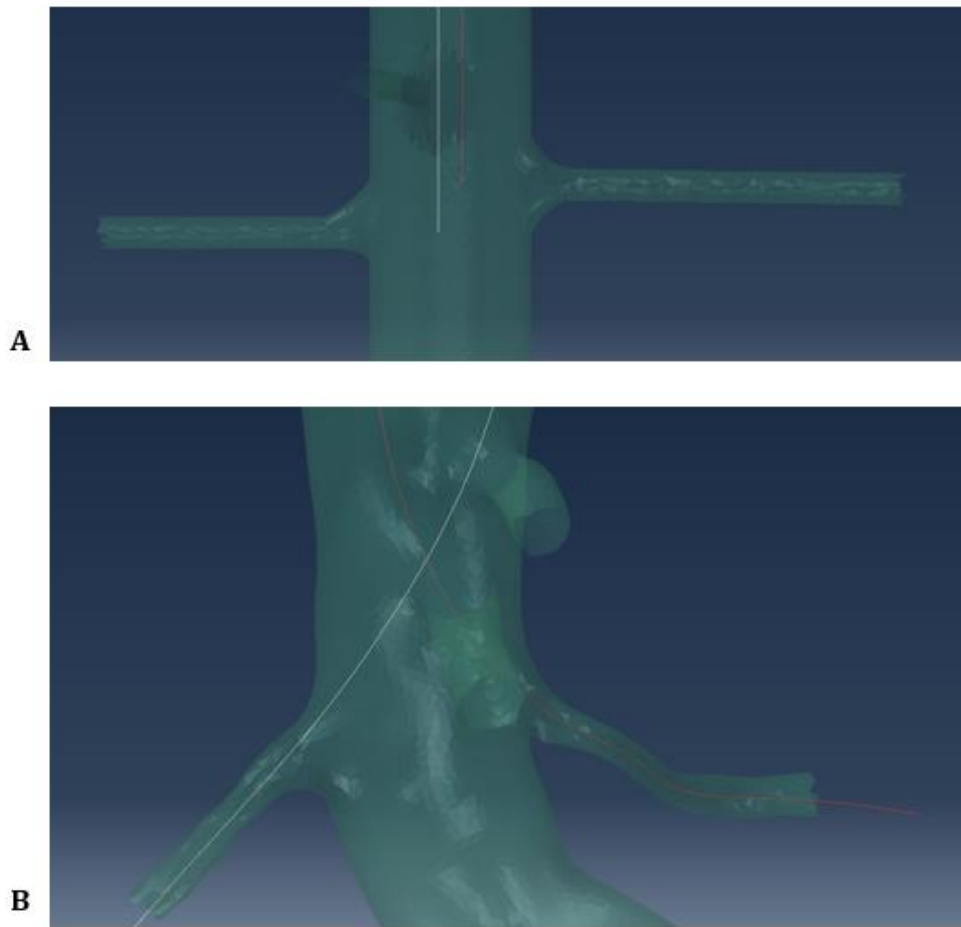


Figure 3.10: (A) zoom guide wires (red and white wires) aligned to the centerlines of the cylindrical arteries; (B) zoom guide wires deployed into the renal arteries of the preoperative model.

The center lines of each artery rotate to the next simpler geometry passing through intermediate positions. The splines and nodes, in turn, change position following the respective center lines and the geometric characteristics of the preoperative model.

The next step is to perform FE element simulation of guide wires insertion in Abaqus software. Guide wires are modeled as linear beam elements and were assigned mechanical properties detailed in table 3.2 obtained from bending test experiments.

Using data extracted from Matlab, guide wires are exactly aligned to the vessels in the cylindrical shape (Fig. 3.10-A).

3.6.3 Guide wires deployment

Then, contact constraint between guide wires and arteries is activated and, setting as BCs the coordinates of the nodes at the final extremities of the renal arteries, the guide wires are inserted in renal arteries (Fig. 3.10-B).

Arteries mesh is then deformed from the most cylindrical shape to the preoperative shape, leading to guide wires deployment in the patient-specific shape geometry.

3.6.4 SG main body, limbs and chimneys modeling

After the guide wires development, the chimneys (Marquet ATRIUM ADVANTA V12 7x32 mm) are built using Matlab by creating a mesh around the deployed guide wires center lines with 4-node quadrilateral surface elements. To build the model of SG main body (Fig. 3.11) and SG limbs, an excel file is completed with the parameters (Tab. 3.2) obtained on the manufacturing company's website.

Table 3.2 - Brand and dimensions in mm of the SG.

	BRAND	PROXIMAL D	DISTAL D	LENGHT
Endograft	Medtronic ENDURANT II ETBF 3216C166E	32	16	166
Right Limb	ETLW 1616C82	16	16	82
Left Limb	ETLW1616C156	16	16	156

A Matlab code uses this excel file (Tab. 3.4) to generate mesh of the stents using linear beam elements.

Stent number	Nb Z	Height	Distal D	Proxi D	Final Distal D	Niti wire D	Wire material	Set	Z coord mid stent
1	5	20	35,57	35,57	32,33	0,33	nitinol	body	9
...

Table 3.3 - The table shows an example of an excel file compiled for the SG main body Stent number: From 1 to 14 in the example (Fig. 3.11), is the number of stents; Nb Z: number of "sine waves" for each stent; Height (mm): stent height for each stent; Set: Body, Bifurcation or legs; Proxi D, distal D, final distal D are the proximal, distal, and final distal diameters (mm) of each set respectively; Niti wire diameter (mm) and wire material are, respectively, the diameter and the material of the stent wire; Z coord mid stent is the Z coordinated in the middle of each stent.

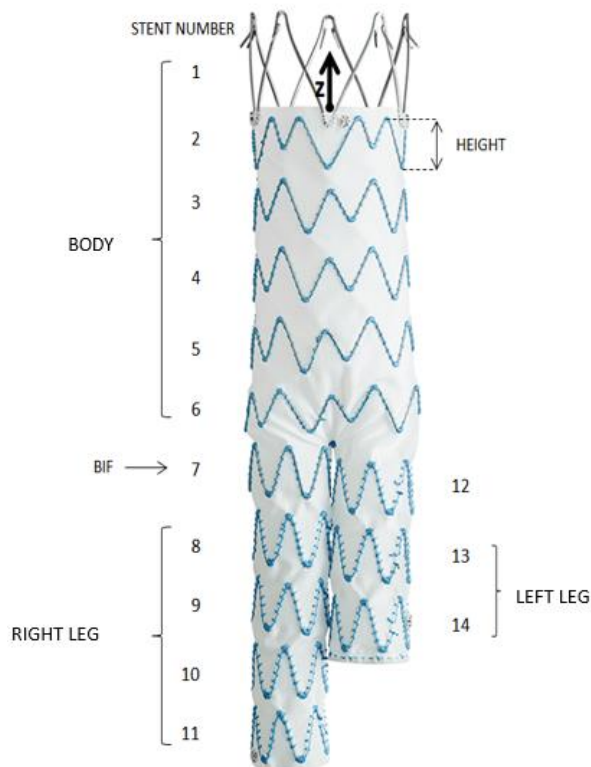


Figure 3.11: Example of SG divided in the main, legs and bifurcation part.

Graft geometry is generated using FreeCAD software and meshed with 4-node linear shell elements. Stents and graft are assigned material properties as detailed below (Table 3.4).

Table 3.4 - Manufacturer mechanical properties (direction 1 = circumferential, direction 2 = axial)

	Material	Type	E₁ [Mpa]	E₂ [Mpa]	G₁₂ [Mpa]	V₁₂
Guide wires	-	elastic	1234	-	-	0.33
Stent	Nitiol	elastic	60000	-	-	0.33
Graft	PET	Elastic orthotropic	1377	4587	14	0.7

3.6.5 SG crimping

As the stents are initially oversized compared to the graft, a simulation as to be performed in Abaqus to crimp them until they are on top of the graft. For cylindrical stents, the stent is crimped by imposing a radial displacement. For non-cylindrical stents, surfaces parallel to those of the graft are crimped until reaching the stent to compress the stents by contact till they reach the graft. (Fig. 3.12)

The same process is applied to build the limbs.

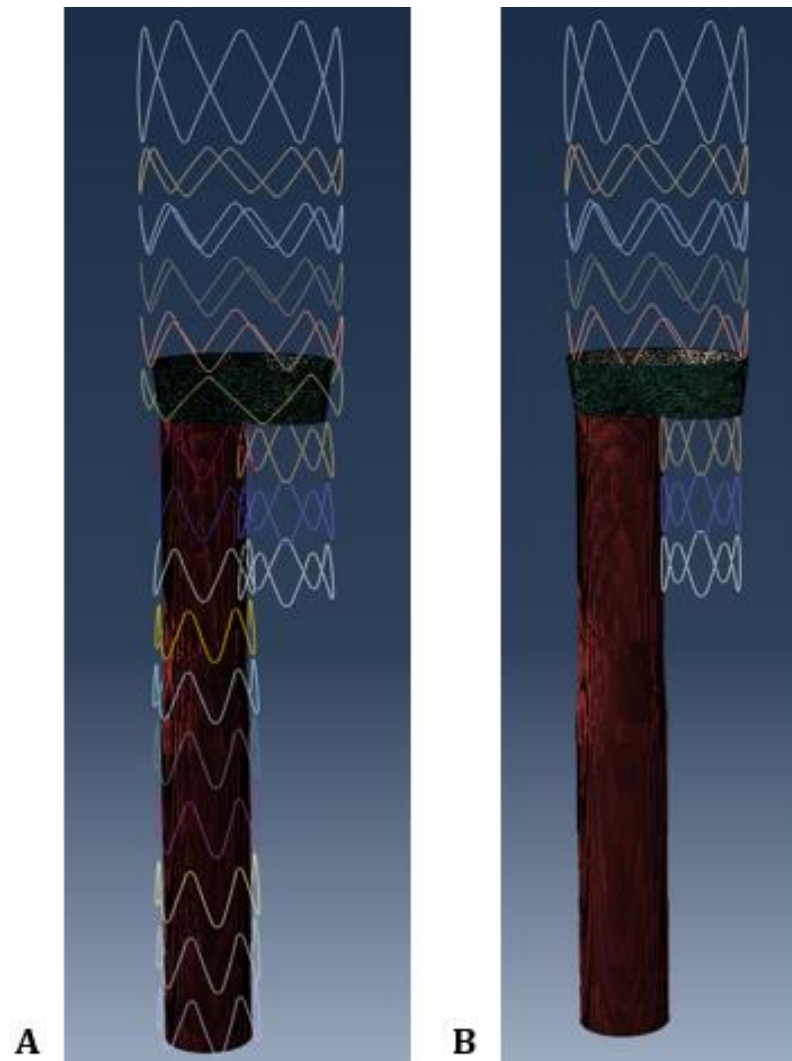


Figure 3.12: SG main body building. (A) Nitinol Stents and graft generated by Matlab input files. (B) Stent and graft crimped in Abaqus.

Then, the limbs are crimped enough to fit inside the proximal SG components. Cylindrical surfaces surrounding parts to be crimped are created, and their diameter is reduced progressively to crimp SG components. For the main body, which have also to be crimped in the following steps to leave enough clearance between its legs for the arterial wall to fit in, 5 cylinders were used simultaneously: one to crimp the upper part, two to crimp the legs and 2 others cylinders inside the previous ones to avoid the overlapping of the crimped limbs with the legs (Fig. 3.13). Crimped limbs are then inserted into the main body (44).

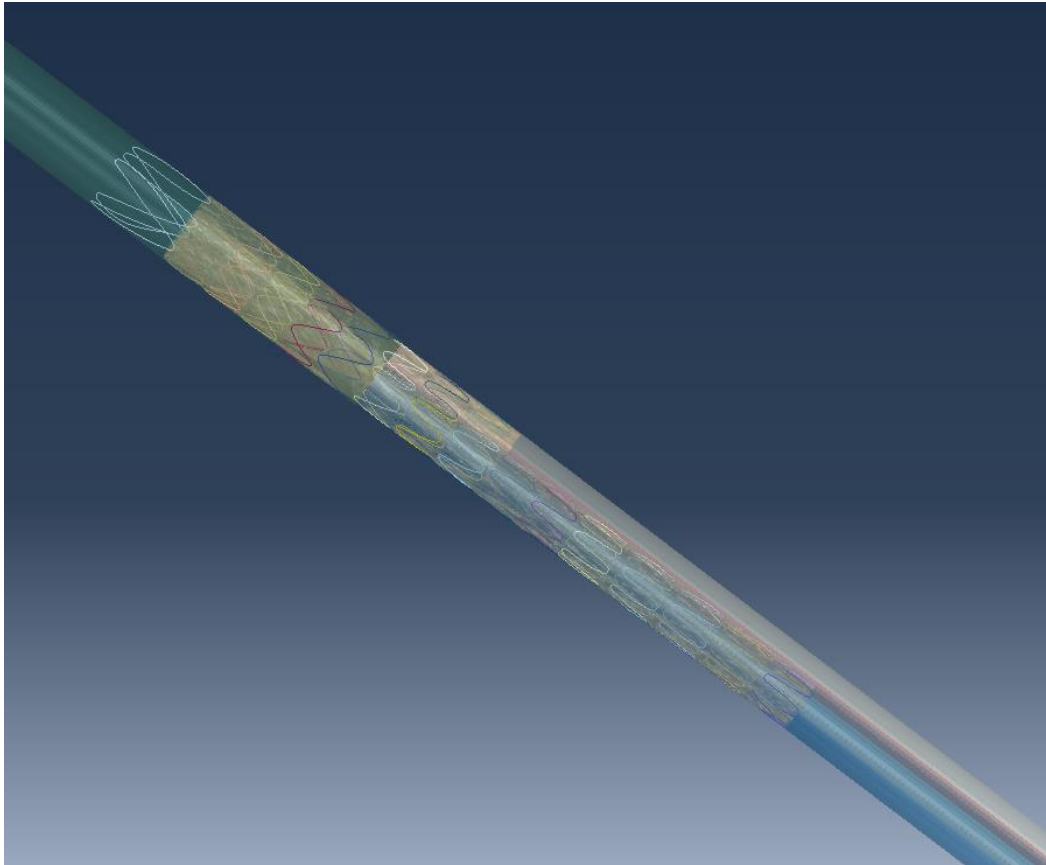


Figure 3.13: SG crimped in the cylinders

3.6.6 Stent placement and deployment

The longitudinal coordinate of the proximal stent (immediately under the mesenteric artery) is defined to guarantee the desired proximal position of the SG, which is determined accordingly to the one observed on the postoperative scan.

The main body, the iliac limbs are first compressed radially and assembled with the chimneys in the cylindrical shape of the aorta. (Fig. 3.14)

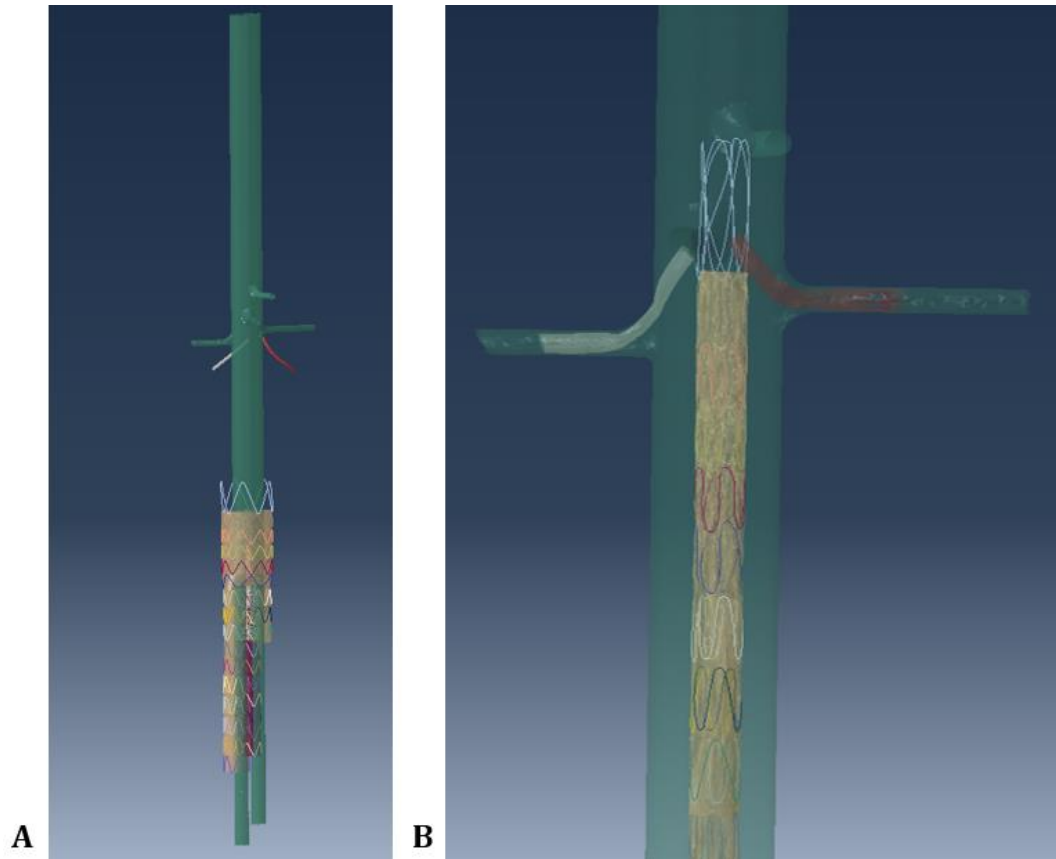


Figure 3.14: (A) Cylindrical aorta, SG main body, limbs and chimneys before deployment. (B) SG Crimped and chimneys in the cylinder shape of the aorta.

Contact constraint is activated between SG components and between SG and aorta. To prevent relative motion between SG components, the value of the friction coefficient was 0.1. Friction between the SG and the arterial wall is modeled using the standard Coulomb friction law with a friction coefficient value of 0.1, in the mid-range of experimental values reported in (45) (“note that a sensitivity analysis proved that friction coefficient value has negligible influence on the results” (45)).

The first simulation step consists in letting the SG deploy inside the aorta in the cylindrical shape.

Then, displacements are applied to every node of the aorta and it is progressively morphed into the preoperative geometry. Contact enforcement constrained the SG to stay inside the aorta during the whole process, preventing the SG from being deployed outside the aneurysm (44).

Finally, all previous kinematical constraints were removed: the vessels were free to be deformed. Only, the nodes at the proximal end of the aorta and at the distal ends of the iliac arteries were clamped. The SG could then recoil and deform the arterial wall until reaching static mechanical equilibrium (Fig. 3.15-A). (44)

“All simulations were carried out with the explicit FE solver of Abaqus software. Time increments (adjusted via mass scaling) and time steps were chosen to obtain fast results while keeping the ratio of kinematic and internal energies under 10% to avoid spurious dynamic effects” (44). (12 CPUs-7h).

FEM simulation allows to extract the fluid domain and the useful data to run the CFD simulation in CRIMSON.

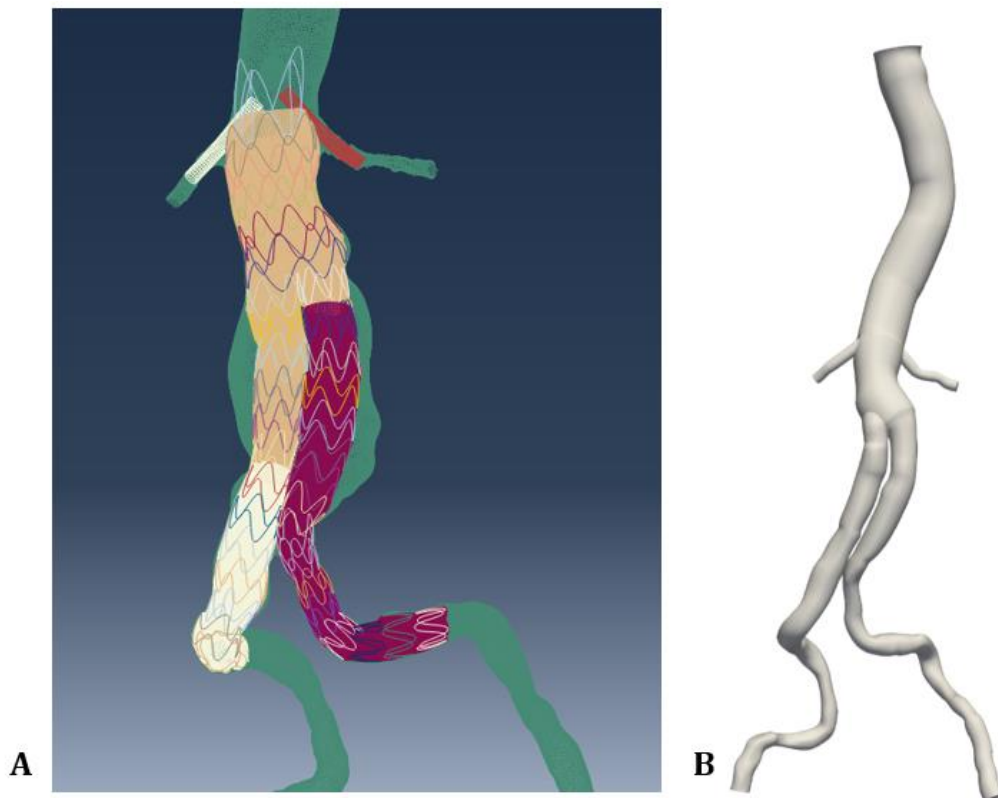


Figure 3.15: (A) SG main body, limbs and chimneys deployed in the preOP model; (B) ch-EVAR model in CRIMSON.

3.7 f-EVAR model without iliac arteries rotation

A second f-EVAR model called in this work “f-ch” is built without evaluate the iliacs rotation for a better hemodynamic comparison. On the stent main-body of the Ch-EVAR, the chimneys have been replaced by the patient-specific fenestrated arteries obtained from CT-scan of the postoperative model.

The technique used to build the Ch-EVAR model simulating the deployment of the stent from the pre-operative scan cannot, indeed, predict the rotation of the iliac arteries.

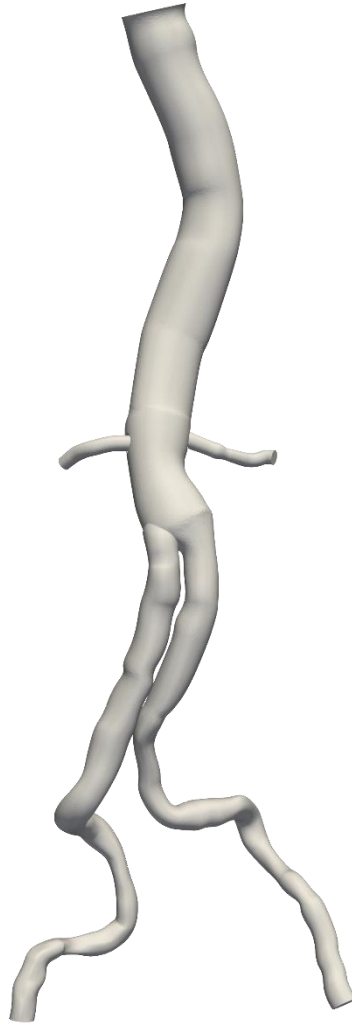


Figure 3.16: f-ch (f-EVAR model without iliac rotation)

3.8 Solver parameters

Built the geometry and set the BCs the simulation is run for 9 cardiac cycles of 0.75 s/cycle. The following solver parameters are used in the last simulation and allow the mesh independence to be achieved.

- Number of Timesteps: 7500
- Time Step Size: 0.0001
- Number of Timesteps between Restarts: 75

3.9 Post-processing

The preoperative and EVAR models are post-processed using ParaView software.

Four cross-sections (Fig. 3.12) were investigated in the renal arteries (proximal, midsection and distal of the stent, and 1 cm after the stent) to study the time average wall shear stress, the velocity and pressure waveforms in the last cardiac cycle. The velocity stream lines and the angles between the renal arteries and the aorta main body are evaluated too.

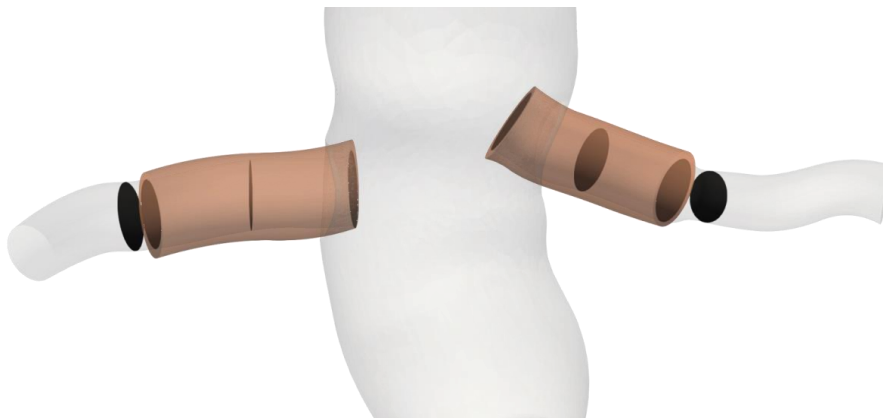


Figure 3.12: f-EVAR model cut in Paraview. The orange color represents the stent and the black one the cross-sections.

3.10 Patient

In this study a preoperative model and 3 postoperative models (f-EVAR, Ch-EVAR and f-ch) were modeled (Fig. 3.13). The model is composed of the abdominal aorta, the two renal arteries and two iliac arteries.

The flow average patient in inlet is 2.7 L/min, the systolic pressure is 128 mmHg and the diastolic pressure is 80 mmHg. The RCRs are in the table below (Tab 3.5):

Table 3.5 – RCRs for each artery. Rp, Rd: $g/(mm^4.s)$ and C: $(mm^4.s^2)/g$

	C	R p	R d
RIA	1,4981	0,0805	0,9754
LIA	1,3567	0,0841	1,0771
RRA	0,8722	0,3338	1,6754
LRA	2,5621	0,2836	0,5703

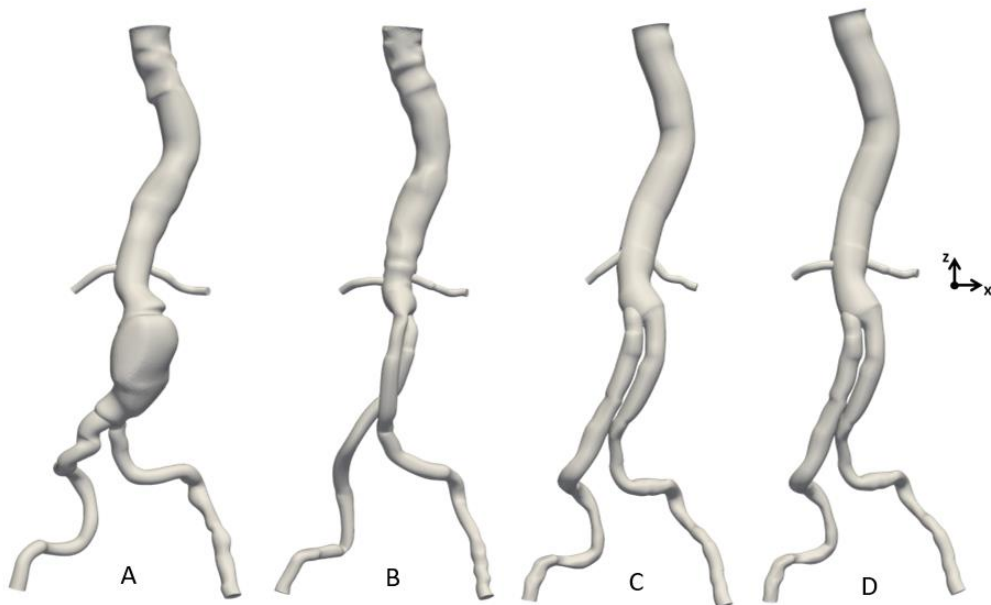


Figure 3.13: Patient-specific abdominal aorta pre-operative (PRE-op [A]) and post-operative (f-Evar [B], ch-EVAR [C], f-ch [D]) models created with CRIMSON

After running the simulations, the models mesh is adapted according to velocity gradient residuals errors.

For each model four mesh adaptations (Tab. 3.6) are necessary to reach the independence.

Table 3.6 – Error reduction factor, minimum and maximum edge size (mm) set to adapt the mesh.

- preOP

	Initial Mesh	1st Mesh Adaptivity	2st Mesh Adaptivity	3st Mesh Adaptivity	4st Mesh Adaptivity
H max	2	2.5	3	2.5	2.5
H min	0.1	0.05	0.04	0.04	0.06
N°Elements	1.5M	800K	1M	2M	4M
Error ratio		0.3	0.3	0.3	0.3

- f-EVAR

	Initial Mesh	1st Mesh Adaptivity	2st Mesh Adaptivity	3st Mesh Adaptivity	4st Mesh Adaptivity
H max	2	3	3	3	3
H min	0.1	0.04	0.05	0.08	0.08
N°Elements	1.5M	850K	1.5M	2M	3M
Error ratio		0.3	0.25	0.3	0.3

- ch-EVAR

	Initial Mesh	1st Mesh Adaptivity	2st Mesh Adaptivity	3st Mesh Adaptivity	4st Mesh Adaptivity
H max	2	3	3	3	3
H min	0.1	0.05	0.05	0.05	0.06
N°Elements	3M	1.5M	2M	3M	4M
Error ratio		0.3	0.3	0.3	0.4

- f-ch

	Initial Mesh	1st Mesh Adaptivity	2st Mesh Adaptivity	3st Mesh Adaptivity	4st Mesh Adaptivity
H max	1.5	3	3	2.5	3
H min	0.1	0.05	0.05	0.05	0.06
N°Elements	2M	1M	1.5M	3M	4M
Error ratio		0.3	0.3	0.3	0.3

4 Results

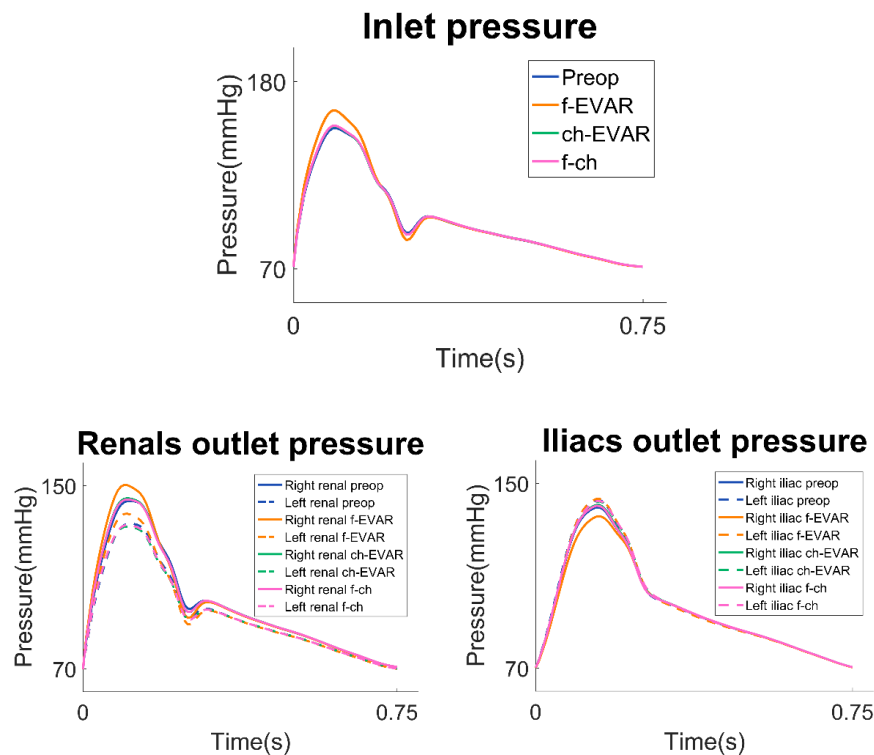
4.1 Hemodynamic in the global model

4.1.1 Pressure waveform analysis

The pressure waveforms at the aorta inlet and at the renal and iliac arteries outlets are compared for all preoperative and postoperative models in the last cardiac cycle.

As shown in the Fig. 4.1 the renal outlets pressure increased in the postoperative models compared with the preoperative, significantly in the f-EVAR one with iliacs rotation. In particular for this model SP and PP increased more than 5% compared to the preoperative and the ch-EVAR one (Tab. 4.2, 4.4).

Figure 4.1: Inlet pressure, renals and iliacs outlet pressure for each model after the simulation.



As predicted, this finding is correlated with the SG implant, which increases the resistance to flow, in particular at the systolic peak.

According to Laplace's law, an increase in pressure lead to an increase in the mean wall stress. Moreover, recent animal studies report that the PP gain influences aortic remodeling: wall thickness, stiffness and axial tension loss (41).

Table 4.1 – Mean pressure (MP) in mmHg and difference (%) between the postoperative and the preoperative models.

	INLET	RRA	LRA	RIA	LIA
Pre-OP	99.8	98.3	94.6	97.0	98.0
f-EVAR	101.2	99.2	95.0	96.1	97.4
ERROR	1.4%	0.9%	0.4%	-0.9%	-0.6%
ch-EVAR	99.9	98.5	94.3	97.2	97.5
ERROR	0.1%	0.2%	-0.3%	0.2%	-0.5%
f-ch	99.9	98.4	94.4	97.1	97.5
ERROR	0.1%	0.1%	-0.2%	0.1%	-0.5%

Table 4.2 - Systolic pressure (SP) in mmHg and difference (%) between the postoperative and the preoperative models.

	INLET	RRA	LRA	RIA	LIA
Pre-OP	158.8	144.8	134.4	140.2	143.5
f-EVAR	170.5	153.5	140.1	136.3	143.9
ERROR	7.4%	6.0%	4.2%	-2.8%	0.3%
ch-EVAR	160.1	146.7	134	141.3	143
ERROR	0.8%	1.3%	-0.3%	0.8%	-0.3%
f-ch	159.9	146	134.5	141	143
ERROR	0.7%	0.8%	0.1%	-0.6%	-0.3%

Table 4.3 - Diastolic pressure (DP) in mmHg and error (%) between the postoperative and the preoperative models.

	INLET	RRA	LRA	RIA	LIA
Pre-OP	70.8	70.6	69.9	70.2	70.2
f-EVAR	68.4	70.6	69.9	70.2	70.1
ERROR	-3.4%	0%	0%	0%	0.1%
ch-EVAR	70.9	70.7	69.9	70.3	70.2
ERROR	0.1%	0.1%	0%	0.1%	0%
f-ch	70.9	70.7	69.9	70.2	70.2
ERROR	0.1%	0.1%	0%	0%	0%

Table 4.4 - Pulse pressure (PP) in mmHg and error (%) between the postoperative and the preoperative models.

	INLET	RRA	LRA	RIA	LIA
Pre-OP	87.9	74.2	64.5	67.0	73.3
f-EVAR	102.1	82.9	70.2	66.1	73.8
ERROR	16.2%	11.7%	8.8%	-1.3%	0.7%
ch-EVAR	89.1	76	64	71	72.6
ERROR	1.4%	2.4%	-0.8%	6.0%	-1.0%
f-ch	89	75.4	64.6	70.7	72.8
ERROR	1.3%	1.6%	0.2%	5.5%	-0.7%

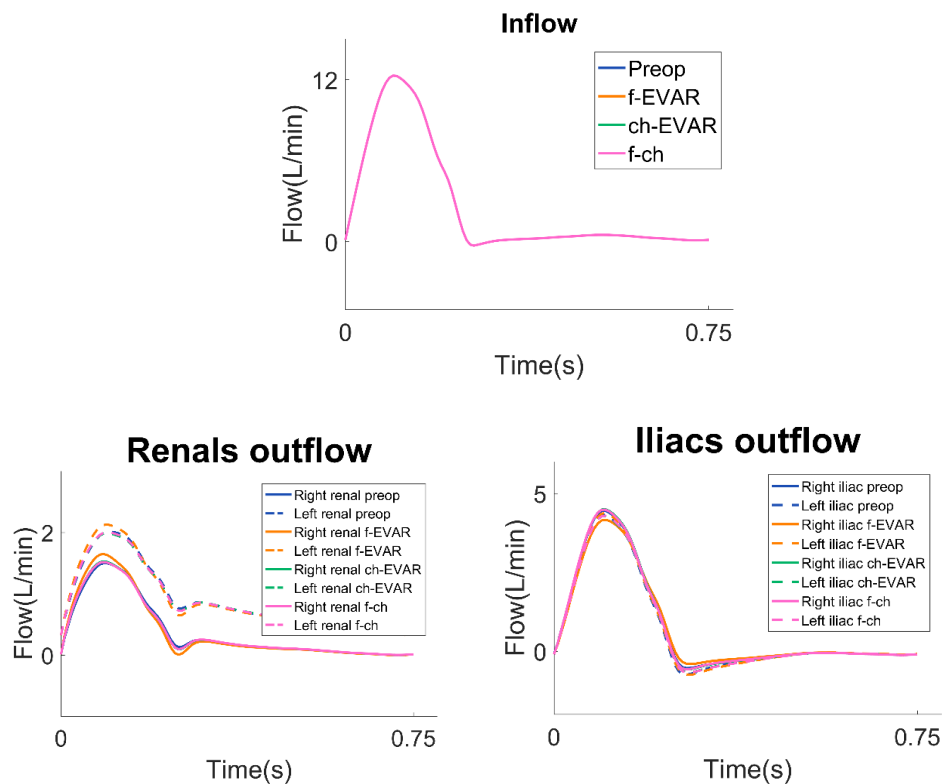
The lack of compliance of the models explains why there is no increase in arteries diastolic pressure (Tab. 4.3) (41).

4.1.2 Flow waveform analysis

The flow waveforms at the aorta inlet and at the renal and iliac arteries outlets are compared for all preoperative and postoperative models in the last cardiac cycle to evaluate the accuracy of the boundary conditions.

The mean flow in inlet is exactly the same, consistent with the mass conservation (Fig. 4.2).

Figure 4.2: Inflow, renals and iliacs outlet flow for each model after the simulation.



Knowing the patient-specific mean flow at the arteries outlets is possible to verify the validity of the BCs set. It is calculated the difference between the patient-specific mean flow and the 3D models mean flow at the outlets after the simulation (Tab. 4.5).

As can be seen from the Table 4.5, the difference between the patient-specific mean flow at each outlet and the models mean flow after the simulation is less than 5%.

Table 4.5 – Mean flow (Qm) in L/min and difference (%) between patient-specific, postoperative and preoperative models.

	INLET	RRA	LRA	RIA	LIA
Patient-specific	2,7	0,394	0,927	0,706	0,642
PreOP	2,7	0,393	0,889	0,737	0,674
f-EVAR	2,7	0,396	0,892	0,731	0,674
ch-EVAR	2,7	0,393	0,886	0,739	0,674
f-ch	2,7	0,393	0,887	0,734	0,674
% PreOP	-	0,4%	4,1%	4,3%	5%
% f-EVAR	-	0,5%	3,8%	3,5%	4,9%
% ch-EVAR	-	0,2%	4,5%	4,7%	5%
% f-ch	-	0,2%	4,4%	4,6%	5%

4.2 Hemodynamic in the renal arteries

4.2.1 Velocity stream-lines distribution

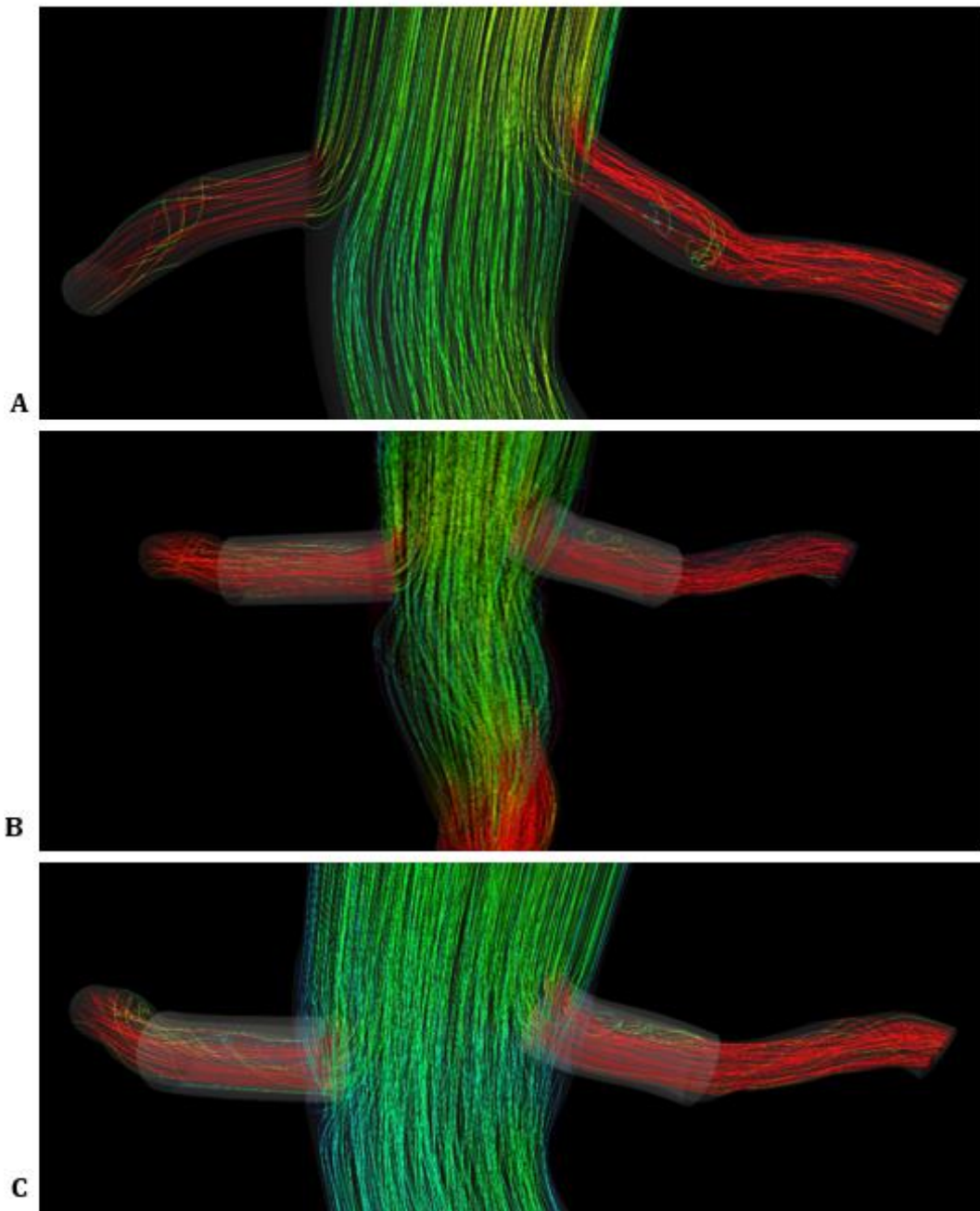
The streamlines are tangential to the velocity vector at every point in the flow at a given instant and forms a powerful tool in understanding flows.

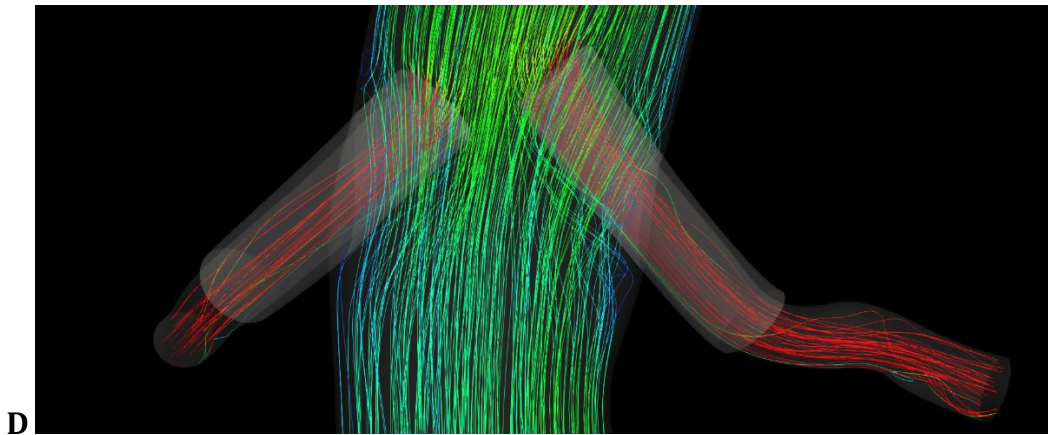
The streamlines at the systolic peak inside the renal arteries of all models are shown in the figure 4.17.

Vorticity is observed in the left renal artery midsection of the preOP model, which extends into fenestrated stents and, instead, disappears after the ch-

EVAR implant. Consequently, the left artery characterized by a high tortuosity affects the flow pattern.

Figure 4.17: Velocity streamlines (A) preOP; (B) f-EVAR; (C) f-ch; (D) ch-EVAR.





Since the presence of vortices that develop in the proximal part of the stent and extend to the distal part, the renal arteries of each model are cut (Fig. 4.3) into four parts (proximal, midsection and distal part of the stent, and 1 cm after the stent) in order to evaluate the velocity and pressure profiles.

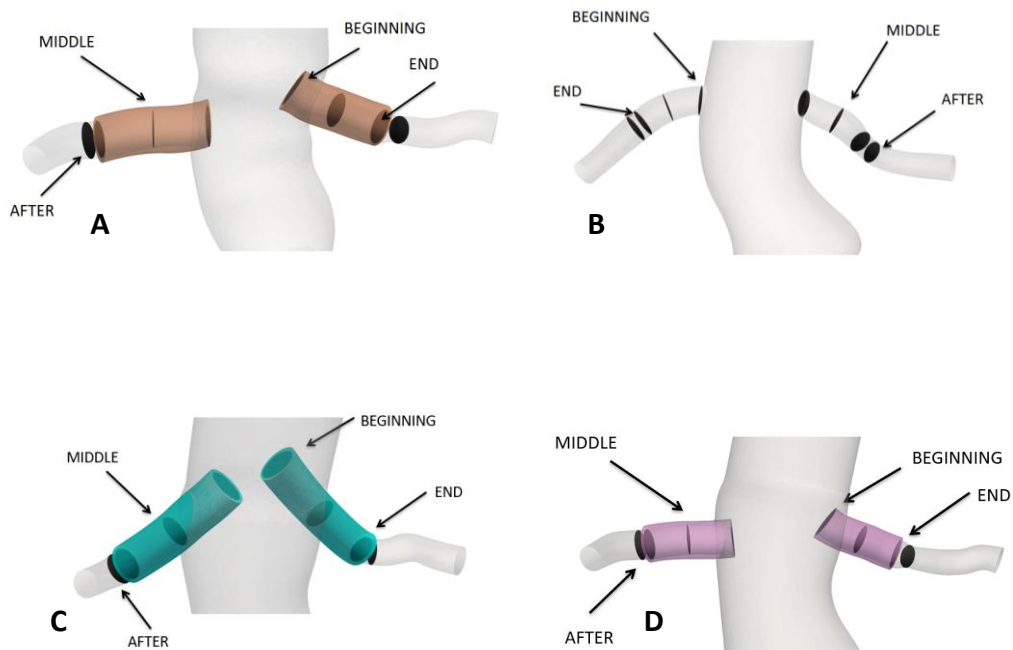


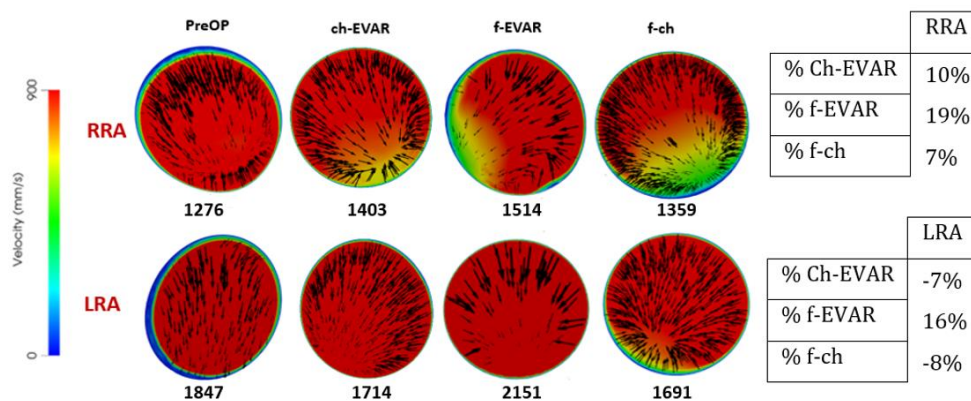
Figure 4.3: (A) Cross-sections in the preOP model; (B) in the f-EVAR model; in the ch-EVAR (C) and in the f-ch (D) models.

4.2.2 Proximal part of the stent

The maximum velocity (Fig. 4.4) increases more than 15% in the f-EVAR model. In particular in the right renal artery characterized by a more linear geometry. Same thing happens with ch-EVAR and f-ch models. In the left renal, instead, with a tortuous geometry there is a velocity decrease for the 2 models without iliacs rotation.

Figure 4.4: Max velocity (mm/s) of the renal arteries in the proximal stent and difference (%) from the preOP model.

The black arrows represent the flux orientation and the number below the slices represent the maximum velocity.



On the other hand, analyzing the trend of pressures (Fig. 4.5), a strong increase in pressure is present both in the patient-specific postoperative model and in the simulated ch-EVAR, due to the stent protrusion in the aorta.

Fig. 4.5: Systolic (SP), Diastolic (DP), Mean (MP) and Pulse (PP) pressure (mmHg) of the renal arteries at the proximal stent and difference (%) between the postoperative and the preoperative models.

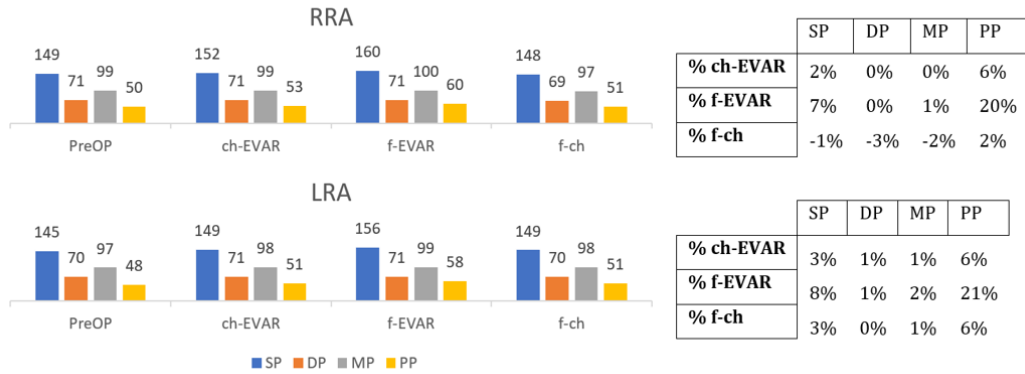
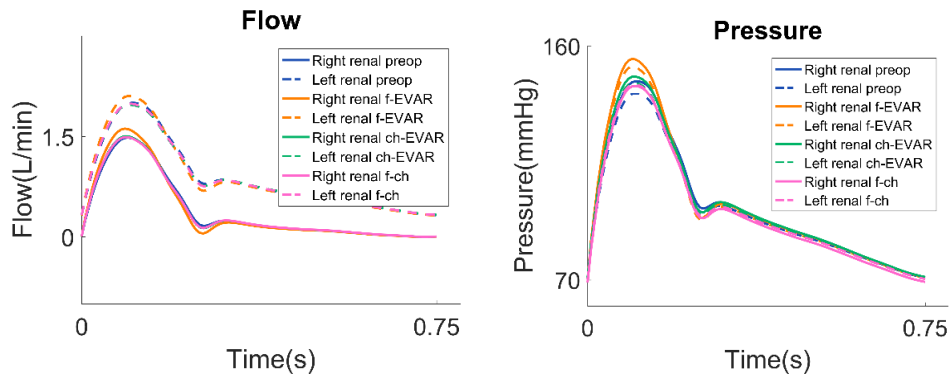


Figure 4.6: Pressure and flow profiles of the renal arteries at the proximal stent.



4.2.3 Stent midsection

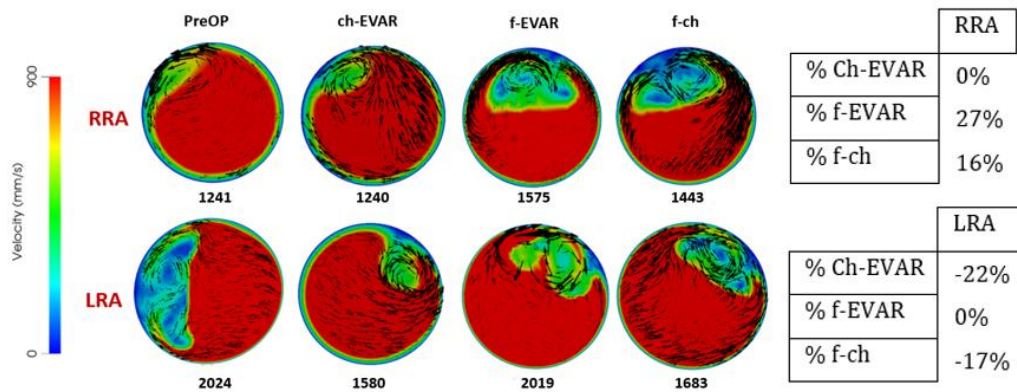
In the midsection of the stent (Fig. 4.7), recirculation zones located on one side can be observed for all the models.

It is interesting to observe that the recirculation zone of the left renal artery changes position in the postoperative models compared to the preoperative

one, while in the right renal artery, on the other hand, a higher recirculation zone is created in the postoperative models.

The max velocity increases in the right renal artery for the fenestrated models and remains instead approximately constant for the ch-EVAR (the percentage errors have been rounded up to the first decimal, so the little variations are neglected).

Figure 4.7: Max velocity (mm/s) of the renal arteries in the midsection of the stent and difference (%) from the preOP model.



In the stent midsection the hemodynamics is very different for the 3 postoperative models. While for the f-EVAR and ch-EVAR model the pressure increases (Fig. 4.8), in the right renal artery of the f-ch model, in which there is a large recirculation zone, the pressure decreases (Fig. 4.9).

Figure 4.8: Systolic (SP), Diastolic (DP), Mean (MP) and Pulse (PP) pressure (mmHg) of the renal arteries in the midsection of the stent and difference (%) between the postoperative and the preoperative models.

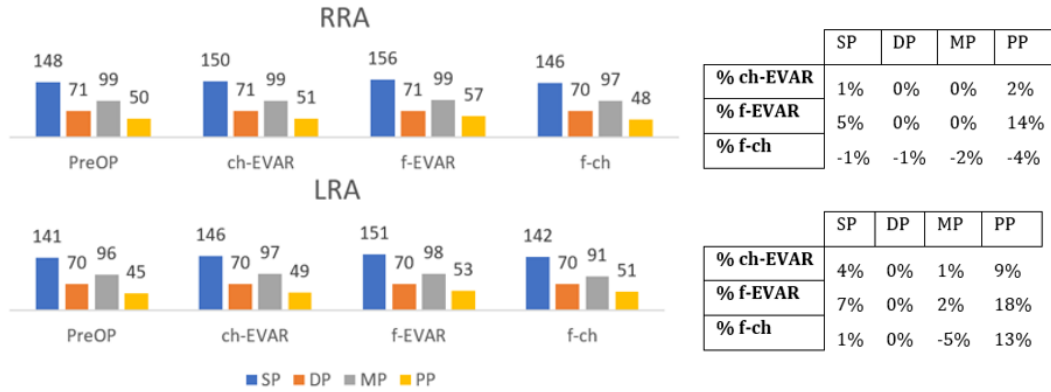
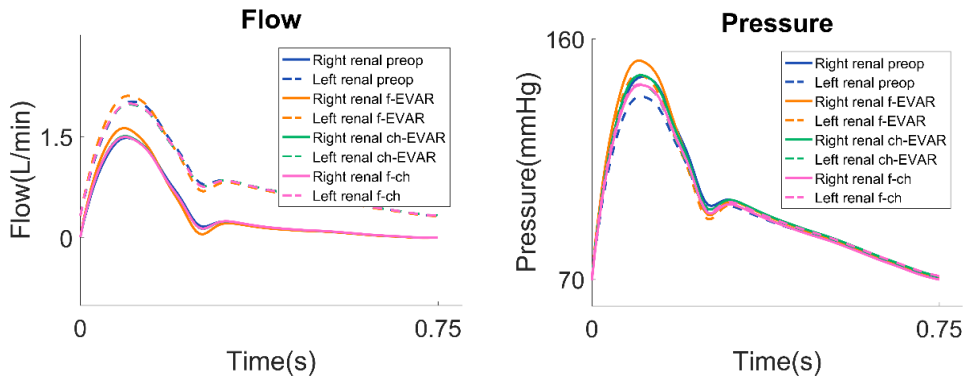


Figure 4.9: Pressure and flow of the renal arteries in the midsection of the stent.

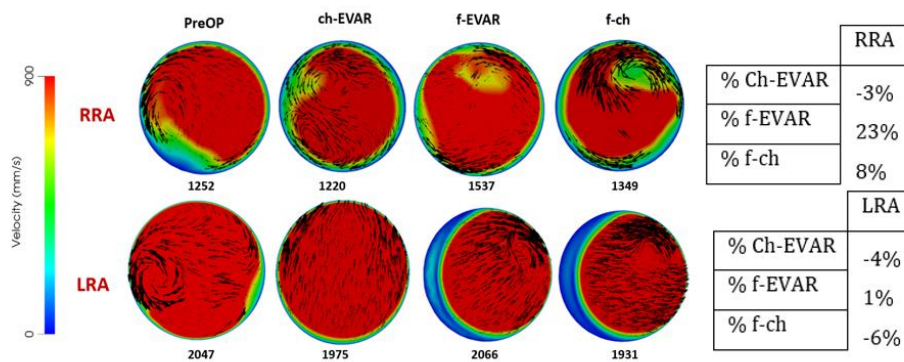


4.2.4 Distal part of the stent

As shown in the Fig. 4.10 and Fig. 4.12 the maximum velocity increases in the fenestrated models in the right renal artery, instead decrease or remain constant in the left one.

It is interesting to note that both the left renal arteries of the fenestrated models present a low velocity area near the stent wall.

Figure 4.10: Max velocity (mm/s) of the renal arteries in the distal stent and difference (%) from the preOP model.



The pulse pressure increases over 10% in the left arteries (Fig. 4.11). In the right renal artery, the difference between the pulse pressure in the patient-specific postOP model is, instead, of 33% compared to the preoperative one.

Figure 4.11: Systolic (SP), Diastolic (DP), Mean (MP) and Pulse (PP) pressure (mmHg) of the renal arteries in the distal stent and difference (%) between the postoperative and the preoperative models.

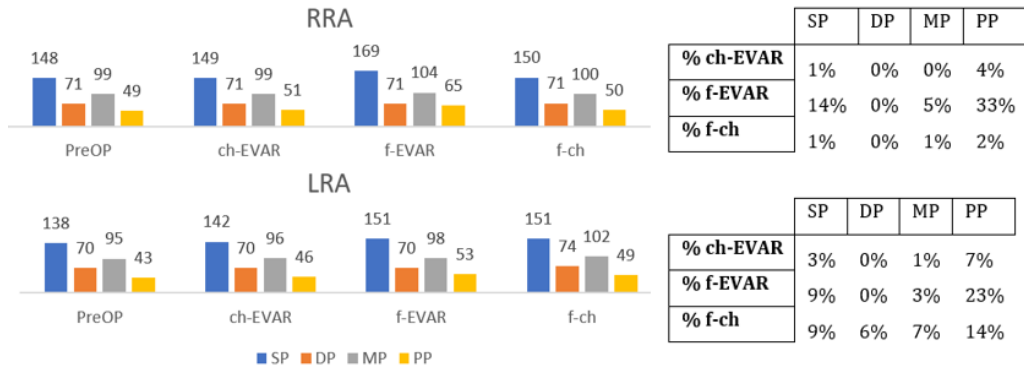
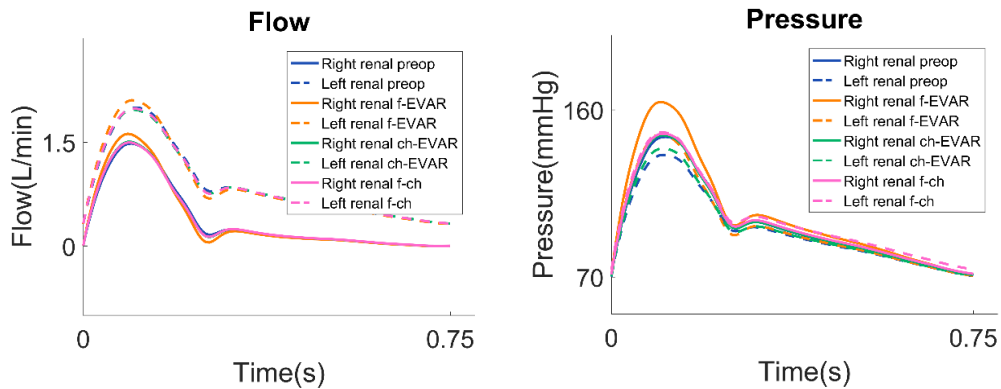


Figure 4.12: Pressure and flow of the renal arteries in the distal stent.



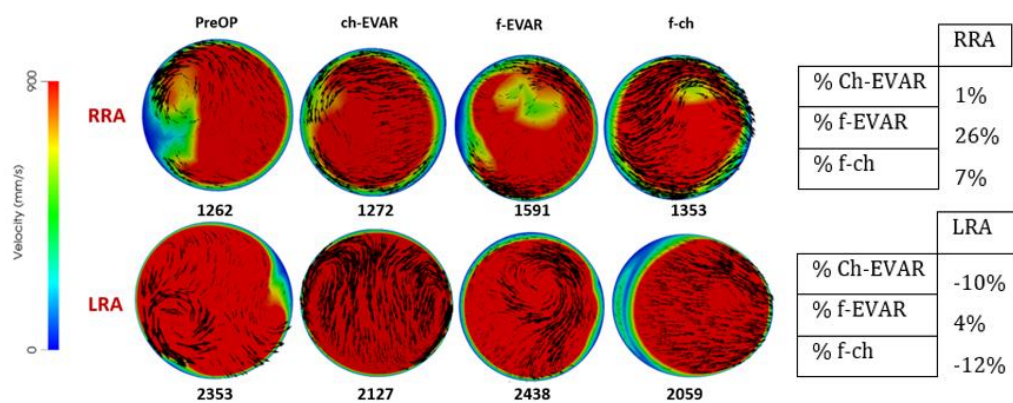
An increase in pressure in all models is evaluated. In particular, by observing the velocity and pressure profiles (Fig. 4.12), the patient-specific postoperative model (orange color) shows a greater hemodynamic difference from the preoperative model.

4.2.5 After the stent

1 cm after the stent (Fig. 4.13), recirculation zones located on one side can be observed in all right renal arteries.

Also, in this case, max velocity increases in the fenestrated model compared to the preOP model, caused by the stents presence that changes the system fluid dynamics. In all the cross-sections the left renal artery velocity is much higher than the right because the patient-specific mean flow is almost double.

Figure 4.13: Max velocity (mm/s) of the renal arteries 1 cm after the stent and difference (%) from the preOP model.



SP and PP increased a lot in the right renal (Fig. 4.14) in the f-EVAR model, probably due to the iliacs twist that that has inevitably changed the preoperative anatomy.

In the left renals SP and PP increase for all the models because of the artery narrowing after the stent exit.

Figure 4.14: Systolic (SP), Diastolic (DP), Mean (MP) and Pulse (PP) pressure (mmHg) of the renal arteries 1 cm after the stent and difference (%) between the postoperative and the preoperative models.

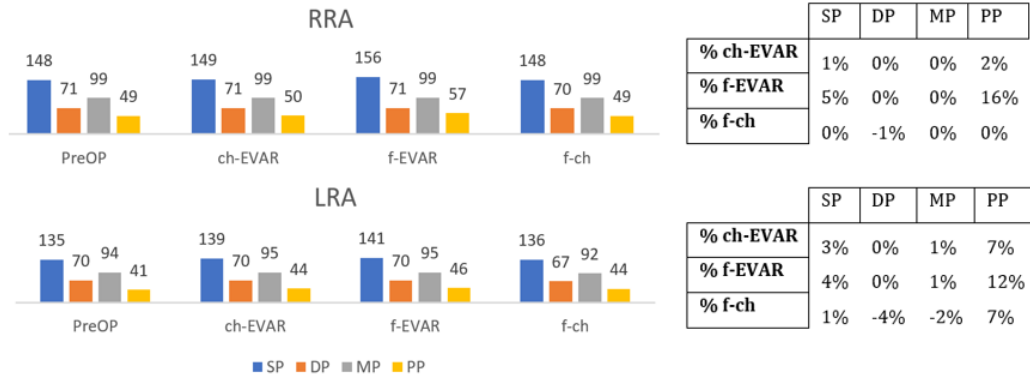
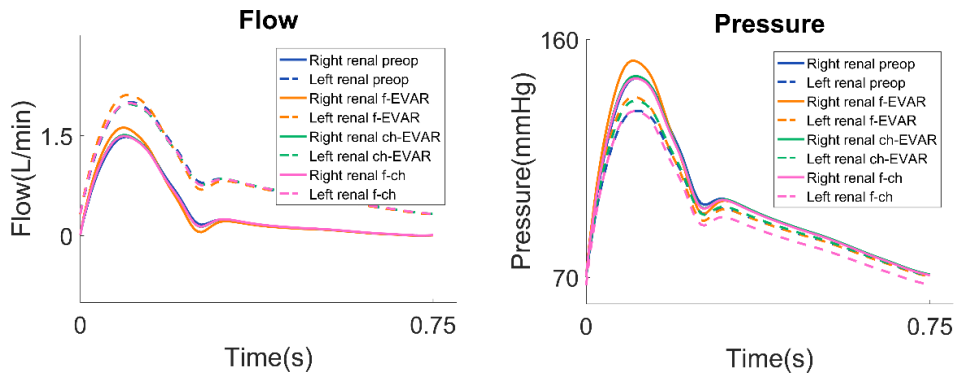


Figure 4.15: Pressure and flow of the renal arteries 1 cm after the stent.



4.3 Wall shear stress analysis

The vessels wall is subject to mechanical forces due to the blood flow. The tangent force to the lumen of the vessel is the wall shear stress that play an important role in the stent performance (26).

A high wall shear stress, also associated with increased intraluminal pressure following stent implant, as seen above, can lead to a failure due to the stent migration (46).

Time average wall shear stress (TAWSS) is used to explore near-wall hemodynamics (Eq. 3.12).

$$\text{TAWSS}(\mathbf{s}) = \frac{1}{T} \int_0^T |\boldsymbol{\tau}_w(\mathbf{s}, t)| dt \quad (3.12)$$

T is the cardiac cycle duration and “s the generic location of the vessel wall” (47).

High WSS is present in the left renal artery (Fig. 4.16), characterized by high tortuosity and an amount of blood flow double than the right artery.

However, areas with lower TAWSS appear in the postoperative models after the stents implant.

TAWSS is applied, in fact, not only to identify areas with high WSS but also to find low WSS areas, which are usually at risk of thrombosis.

The right renal artery in all models presents a TAWSS close to the lower physiological limit, in this artery there is a more linear geometry and a much lower mean flow than the left renal artery.

The WSS physiologically varies from 1 to 7 Pa, whereas atherosclerosis-prone regions exhibit TAWSS < 0.4 Pa. Non-physiologically high WSS, however, has been reported to be >7 Pa, usually seen in severe stenosis (44).

Looking at the TAWSS color map we note that there is a low WSS area immediately after the stent of all models. The EVAR technique in fact changes the native geometry.

Tasso et al. (47) showed a correlation between some geometric descriptors of torsion and curvature, and the volume of recirculation flow.

The ch-EVAR model has the lowest AWSS (Eq. 3.13) in the arteries (Tab. 4.6). In the chimney technique, in fact, the blood flow is suddenly forced from the main body to a perpendicular exit through the renal arteries. This new geometric complexity after the stent implant is often related to a thrombogenic tendency (47) and needs surgical reintervention.

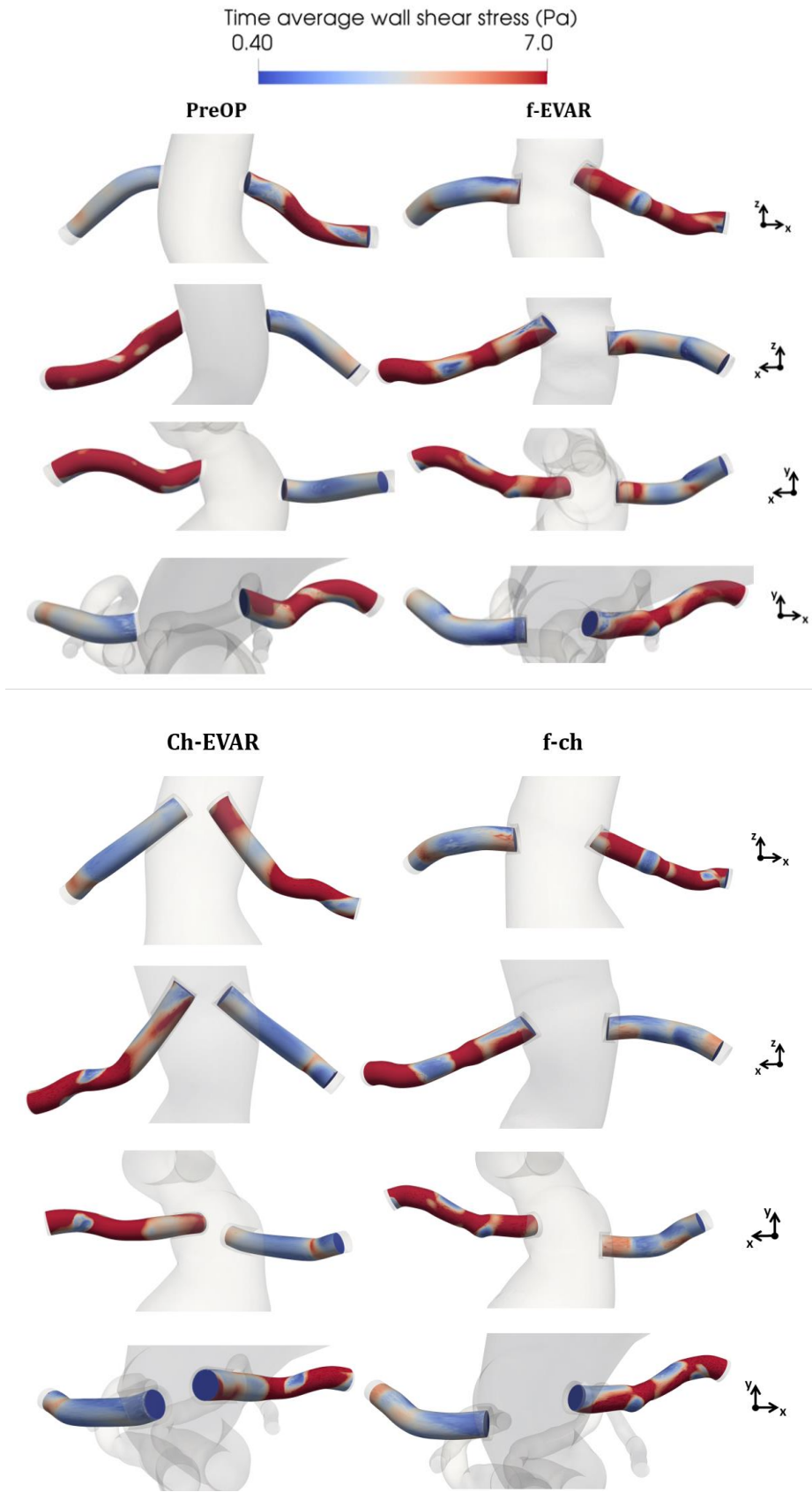


Figure 4.16: TAWSS in the renal arteries.

To locate the WSS, the renal arteries are divided into two parts (just distal artery area and total artery: stent + distal artery) and the TAWSS averaged (Eq. 3.13) on the luminal surface S is calculated (Tab. 4.6).

$$AWSS = \frac{1}{S} \int_S TAWSS(s) \, dS \quad (3.13)$$

Table 4.6 – AWSS (Pa) in the PreOP and postoperative models

PreOP		f-EVAR		Ch-EVAR		f-ch	
	AWSS	RRA		RRA		RRA	
			AWSS		AWSS		AWSS
		Artery+stent	2,89	Artery+stent	2,28	Artery+stent	2,71
		Distal artery	2,25	Distal artery	2,50	Distal artery	2,89
		LRA		LRA		LRA	
			AWSS		AWSS		AWSS
RRA	2,76	Artery+stent	7,73	Artery+stent	6,99	Artery+stent	7,60
LRA	8,96	Distal artery	9,15	Distal artery	9,61	Distal artery	8,99

The TAWSS distribution at the luminal arteries surface underlines that the f-EVAR with iliacs rotation presented the highest AWSS values between the postoperative models.

By dividing the stent into two parts it is shows that the high WSS is concentrated in the distal part of the artery. As previously seen, in fact, in the stent midsection there is a large recirculation zone, which can “cause the incidence of intra-prosthetic thrombus deposits” (47). Consequently, a stent downstream pressure increases and a greater displacement force on the endograft is applied, cause of migration and endoleak.

4.4 Evaluation of renal arteries angulation before and after stent implant

The durability of stent grafts may be related to how procedures and devices alter native anatomy. It is aimed to quantify and compare renal artery geometry before and after endovascular aneurysm repair.

The angle between the renal arteries and the aorta's centerline in the coronal plane and the angle between the renal arteries and a vertical axis passing through the center of the aorta in the axial plane were measured (Tab. 4.7) processing the CT-scans with the ImageJ and Paraview softwares (Fig. 4.15).

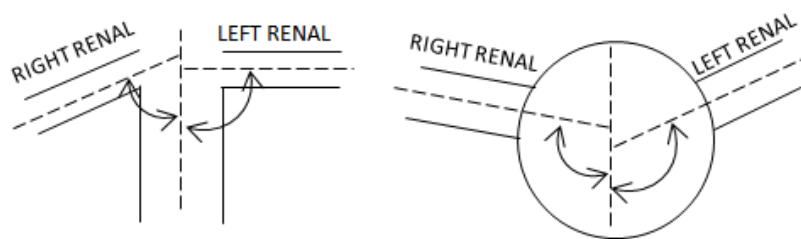


Figure 4.18: Scheme of the method used to calculate the angles.

In the coronal plane f-EVAR induced significantly great angle change (Tab. 4.8) at the stent and curvature change distal to the stent compared to the preOP model. “These differences may exert differential effects on long-term renal artery patency, integrity, and renal function following complex EVAR” (48) for abdominal aortic aneurysms.

In the Ch-EVAR stent, instead, a higher change in the axial plane angles is present, since the chimneys implant is parallel to the stent main body. This doesn't create in-stent vorticity as seen before in the streamlines analysis, since there is no sudden change in flow direction at the beginning of the stent, but this stent greatly changes the native arteries geometry, which can lead to a higher chance of second intervention.

Table 4.7- PreOP and PostOP agles measured in both renal arteries.

	pre-op	f-EVAR	Ch-EVAR	pre-op	f-EVAR	Ch-EVAR
	RR	RR	RR	LR	LR	LR
Axial	89°	85°	44°	90°	92°	35°
Coronal	51°	90°	75°	61°	70°	83°

Table 4.8 – Difference between angles in the PreOP and postOP models for both renal arteries.

	f-EVAR		Ch-EVAR	
	RR	LR	RR	LR
Axial	4°	2°	45°	55°
Coronal	39°	15°	24°	22°

“Timing of pre- and postoperative imaging was also not standardized, thereby limiting the ability to compare the long-term geometric changes” (48).

The manually technique to obtain the angles from the CT-scan presents operator dependent errors, so it would be useful to neglect the errors under 10°.

5 Discussion

5.1 State of the art and achievements

In this study, a preoperative model and three models of the endoprosthesis (f-EVAR, f-ch and ch-EVAR), used for the treatment of abdominal aortic aneurysms, are built. The patient-specific preoperative and fenestrated postoperative (f-EVAR) models are built using CT-scans, while the ch-EVAR model is built using an innovative methodology that simulates the chimneys deployment within the renal arteries through the preoperative patient-specific CAD.

Finite-element analysis (FEA) could help, in fact, predicting “SG positioning inside patient-specific AAA, thus enabling surgeons to anticipate complications” (44). Several teams started to focus on “EVAR long term outcomes through fluid dynamics to estimate the blood mechanical action onto SGs” (44).

“Despite their major interest, these studies present the following limitations: (i) they do not take into account SG deployment and (ii) most of them use over simplified SG models” (44).

The technique used to build the Ch-EVAR model simulating the deployment of the stent from the pre-operative scan cannot predict the rotation of the iliac arteries.

Therefore, a second fenestrated model is built without evaluate the iliacs rotation for a better hemodynamic comparison. On the stent main-body of the Ch-EVAR, the chimneys have been replaced by the fenestrated arteries.

The aim of the work is to compare the local hemodynamics between the EVAR and the preoperative models in order to study the associated clinical impact.

“The purpose of implanting a stent-graft is to exclude the aneurysm from the systemic blood circulation, for this purpose there is no difference between the

conventional aortic stent graft and the fenestrated stent graft. The unique characteristics of the fenestrated stent graft involve the creation of an opening in the graft material by inserting fenestrated stents into the renal arteries. Furthermore, a fenestrated stent normally protrudes into the aortic lumen. Therefore, there is a potential risk for fenestrated stents to interfere with renal blood flow” (49).

However, Sun Zhonghua et Chaichana Thanapong (49) didn't observed significant changes in the calculated velocity of the renal arteries following implant of fenestrated stents in their study. “Flow recirculation or a vortex was observed at the proximal renal arteries because of the intra-aortic protruded stent” (49). Nonetheless, the effect of fenestrated stents on the renal velocity was insignificant.

In this study, however, the impact of the stent leads to a vortex creation in the proximal part of the fenestrated stents that extends to the distal stent. Therefore, dividing the model into cross-sections, it is noted the presence of a large recirculation area in the stent midsection. These areas usually characterized by low WSS contributes to complications immediately after the fenestrated stents implant. Generally, the induction of intimal hyperplasia, in-stent remodeling and thrombus formation.

A decrease in the maximum velocity is also present in the left renal artery of the two simulated models without iliac rotation, characterized by elevated tortuosity and curvature. A stagnation area is also present in the distal part of the fenestrated stents. These areas, besides being thrombogenic, cause an increase in downstream pressure, which can lead to stent migration and complications associated with the risk of a second reintervention, such as endoleak.

The geometric complexity associated with the stent implant is reflected indirectly on the renal arteries even after the iliac rotation present in the patient-specific postoperative model.

Indeed, a complication of the fenestrated endovascular aneurysm repair is the potential rotation of the stent during the SG deployment which can lead to arteries occlusion (50).

According to Doyle et al. (51) this rotation is caused by an accumulation of rotational energy when the device is deployed through the iliac arteries and by characteristics of the iliac artery, such as the high torsion or the presence of calcifications.

In the f-EVAR model there is the highest hemodynamic variation compared to the simulated models, especially differences in pressure.

In all postoperative models, in fact, there is a change in pressure due to the stent protrusion inside the main body but in the case of the iliac rotation model the pulse pressure increased always over 10%.

“Recent animal studies (52), (53) have identified the strong role of PP in aortic remodeling, specifically wall thickening, stiffening, and loss of axial tension” (41). Changes pressures directly affects wall stress and renals failure.

“Howell et al. (54) showed that pressure-related forces at the graft bifurcation have a major impact on graft endoleak or migration risk. Figueroa et al. (55), (56) concluded that EVAR migration or movement is a result of pulsatile displacement forces which are related to endograft geometry and curvature” (57).

As previously reported, this increase in pressure change the forces on the stent and therefore the risk of migration and endoleak.

Furthermore, an uncontrolled increase as in the fenestrated with iliacs rotation and a high WSS could lead to direct endothelial injury.

5.2 Limitations and future development

Our study investigates the hemodynamic effect of fenestrated stents on the renal arteries on one sample patient. Thus, it would be useful to apply this methodology to other patients to have robust results. In the patient-specific model the walls were assumed as rigid rather than elastic for time efficiency reasons. In fact, simulations can be very long (some may take 60 CPU-120h). In the normal physiological situation, the artery wall moves with the cardiac cycles, so we must consider that the WSS values could be affected by this hypothesis.

Chen et al. (58) showed that considering blood as a Newtonian fluid does not significantly change the results.

A simulation of various lengths of stent protrusion is needed so that a robust conclusion can be drawn.

Methodology has to be improved to ensure equivalence of segmentations generated by VMTK and Crimson (by varying parameters used in VMTK for example) or to be able to use one of these segmentations as input of both f-EVAR and ch-EVAR simulations.

More studies to also predict the iliac rotation by preoperative CT-scan, to obtain the correct stent deployment, would lead to a better hemodynamic comparison.

6 Conclusion

Endovascular aortic repair (EVAR) is an effective alternative to conventional open surgical repair to treat the geometry aneurysms of the abdominal aorta. In this work we carried out numerical simulation to predict the impact of these interventions by modelling pre and post-intervention hemodynamic.

Postoperative complications, caused by the fenestrated and chimneys implant, can lead to hemodynamic changes especially in the renal arteries.

Using patient-specific models, the hemodynamic between the postoperative and preoperative models is compared.

The stent protrusions inside the aorta lead to a consistent increase in pressure, in particular in the iliac rotation model.

The altered native geometry of the stent can lead to new forces that can cause complications such as stent migration or endoleak. Not only the protrusion but also the higher geometric complexity, given by new levels of torsion and curvature in the renal arteries, leads to a decrease in the local velocity and an increase in the downstream pressure, with possible consequent stent failure.

The low WSS areas present after the stent can lead to the induction of thrombogenic pathways, while the recirculation zones present in the stent midsection increase the risk of NIH formation and aortic remodeling with consequent downstream pressure drop.

Despite some hemodynamics features in the chimneys model simulated without iliac rotation and the patient-specific fenestrated model in which the iliac rotation is present are comparable, it would be necessary to find a method in order to also predict the correct deployment of the iliac arteries starting from the preoperative CT-scan.

The introduction of the stents has led to an innovation in the world of cardiovascular surgery, contributing to a significant reduction in post-stent

complications. However, the clinical failures associated with thrombosis and therefore the slow degradation of renal function in ch-EVAR; restenosis, due to neointimal hyperplasia as a first reaction to the fenestrated stent implant (27), explains how CFD, as a mathematical tool, can help to understand the physical phenomena of flow within an artery and prevent postoperative complications .

7 References

1. Collins, Jarrod A., et al. The anatomy of the aging aorta. *Clinical Anatomy*. 7, 12 February 2014, Vol. 27, pp. 463-466.
2. Miller-Keane. aorta. *Encyclopedia and Dictionary of Medicine, Nursing, and Allied Health, Seventh Edition*. [Online] 2003. <https://medical-dictionary.thefreedictionary.com/aorta>.
3. Hoffman, Matthew. Human Anatomy. *WebMD*. [Online] <https://www.webmd.com/heart/picture-of-the-aorta#1>.
4. Hill, M.A. Embryology HM Practical - Blood Vessel Histology. [Online] https://embryology.med.unsw.edu.au/embryology/index.php/HM_Practical_-_Blood_Vessel_Histology.
5. Erbel R, Eggebrecht H. Aortic dimensions and the risk of dissection. *Heart*. 2006, Vol. 92, 1, pp. 137-42.
6. Ambroise Duprey, Olfa Trabelsi, Marco Vola, Jean-Pierre Favre, Stéphane Avril. Biaxial rupture properties of ascending thoracic aortic aneurysms. *Acta Biomaterialia*. 2016, Vol. 42, pp. 273-285.
7. Ali, Chehab. *Biomechanical Simulation of Chimney-EVAR technique For Aortic Aneurysm Treatment*. Pavia : s.n., 2016/2017.
8. Lasheras, Juan C. The Biomechanics of Arterial Aneurysms. *Annual Review of Fluid Mechanics*. 2007, Vol. 39, pp. 293–319.
9. Jonathan L. Eliason, Gilbert R. Upchurch Jr. Endovascular Treatment of Aortic Aneurysms: State of the Art. *Current Treatment Options in Cardiovascular Medicine*. 2009, Vol. 11, pp. 136–145.
10. BaptistHealth. Abdominal aortic aneurysm. [Online] <https://www.baptistjax.com/health-library/disease/abdominal-aortic-aneurysm>.

11. Salem, M.K. et al. Should Asian Men be Included in Abdominal Aortic Aneurysm Screening Programmes? *Eur J Vasc Endovasc Surg.* 2009, Vol. 38, 6, pp. 748 - 749.
12. Suvrano De, Farshid Guilak, Mohammad Mofrad. *Computational Modeling in Biomechanics.* s.l. : Springer Netherlands, 2010, 2010.
13. Sheps, Sheldon G. Doppler ultrasound: What is it used for? *Mayo Clinic.* [Online] <https://www.mayoclinic.org/doppler-ultrasound/expert-answers/faq-20058452>.
14. Yolanda Bryce, Philip Rogoff, Donald Romanelli, Ralph Reichle. Endovascular Repair of Abdominal Aortic Aneurysms: Vascular Anatomy, Device Selection, Procedure, and Procedure-specific Complications. *Radiographics.* 2015, Vol. 35, 2, pp. 593-615.
15. Wang LJ, Prabhakar AM, Kwolek CJ. Current status of the treatment of infrarenal abdominal aortic aneurysms. *Cardiovasc Diagn Ther.* 2018, Vol. 8, Supp 1, pp. S191-S199.
16. Parodi, J.C., Palmaz, J.C., and Barone, H.D. Transfemoral intraluminal graft implantation for abdominal aortic aneurysms. *Ann Vasc Surg.* 1991, Vol. 5, pp. 491-499.
17. Andrew England, Richard McWilliams. Endovascular Aortic Aneurysm Repair (EVAR). *Ulster Med J.* 2013, Vol. 82, 1, pp. 3-10.
18. Ricotta JJ 2nd, Oderich GS. Fenestrated and branched stent grafts. *Perspect Vasc Surg Endovasc Ther.* 2008, Vol. 20, 2, pp. 174-87.
19. LaFlamme, David. *Cardiology, a practical Handbook.* Paris : FRISON-ROCHE, 2016.
20. Boulton, M. et al. Predictors of Success Following Endovascular Aneurysm Repair: Mid-term Results. *European Journal of Vascular and Endovascular Surgery.* Vol. 31, 2, pp. 123 - 129.

21. Mayo Clinic. Endovascular repair of complex aortic aneurysms. *Mayo Clinic*. [Online] <https://www.mayoclinic.org/medical-professionals/cardiovascular-diseases/news/endovascular-repair-of-complex-aortic-aneurysms/mac-20429867>.
22. Hila Ben Gur, Moses Brand, Gábor Kósa and Saar Golan. *Computational Fluid Dynamics of Blood Flow in the Abdominal Aorta Post "Chimney" Endovascular Aneurysm Repair (ChEVAR)*. 2017.
23. Lombardo, Agostino. *Indagine diagnostica sulle complicanze in seguito a un intervento di Endoprotesi per aneurisma dell'aorta addominale: L'Endoleak*. 2009/2010.
24. Brian C. Gardner, Saher S. Sabri. *IR Playbook - Endoleak*. s.l. : Springer, 2018. pp. 219-227.
25. Peter R. Taylor, John Reidy, John E. Scoble. Endovascular abdominal aortic aneurysm repair and renal function. *Nephrology Dialysis Transplantation*. 2006, Vol. 21, 9, pp. 2362–2365.
26. Timmins, Lucas H, et al. Increased artery wall stress post-stenting leads to greater intimal thickening. *Laboratory Investigation*. 2011, Vol. 91, pp. 955–967.
27. Nandini Duraiswamy, Richard T. Schoephoerster, Michael R. Moreno, James E. Moore Jr. Stented Artery Flow Patterns and Their Effects on the Artery Wall. *Annual Review of Fluid Mechanics*. 2007, Vol. 39, pp. 357-382.
28. Cavallini, Claudio. *Fattori clinici, angiografici e procedurali predittivi di restenosi coronarica dopo impianto di stent: sintesi delle evidenze*. Divisione di Cardiologia, Dipartimento Cardiovascolare, Ospedale Regionale Ca' Foncello. Treviso : s.n.
29. Walker, T. Gregory et al. Clinical Practice Guidelines for Endovascular Abdominal Aortic Aneurysm Repair: Written by the Standards of Practice Committee for the Society of Interventional Radiology and Endorsed by the

Cardiovascular and Interventional Radiological Society of Europe. *Journal of Vascular and Interventional Radiology*. Vol. 21, 11, pp. 1632 - 1655.

30. H. Meng, V.M. Tutino, J. Xiang and A. Siddiqui. High WSS or Low WSS? Complex Interactions of Hemodynamics with Intracranial Aneurysm Initiation, Growth, and Rupture: Toward a Unifying Hypothesis. *American Journal of Neuroradiology*. 2014, Vol. 35, 7, pp. 1254-1262.

31. CRIMSON. CRIMSON (CARDIOVASCULAR INTEGRATED MODELLING & SIMULATION). [Online] <http://www.crimson.software/>.

32. Figueroa, C. Alberto, et al. A coupled momentum method for modeling blood flow in three-dimensional deformable arteries. *COMPUTER METHODS IN APPLIED MECHANICS AND ENGINEERING*. 2006, Vol. 195, 41-43, pp. 5685-5706.

33. Youssefi P, Sharma R, Figueroa CA, Jahangiri M. Functional assessment of thoracic aortic aneurysms - the future of risk prediction? *Br Med Bull*. 2017, Vol. 121, 1, pp. 61-71.

34. Lantz, Jonas. *On Aortic Blood Flow Simulations*. Linköping, Sweden : Department of Management and Engineering, 2013.

35. Campo-Deaño L, Oliveira MN, Pinho FT. A Review of Computational Hemodynamics in Middle Cerebral Aneurysms and Rheological Models for Blood Flow. *Appl. Mech. Rev.* 2015, Vol. 67, 3, pp. 030801-16.

36. Anne M. Robertson, Ad'elia Sequeira, and Robert G. Owens. Rheological models for blood. [Online]

37. Fung, Y.C. *Biomechanics Circulation*. s.l. : Springer, 1997.

38. What is Viscosity? [Online] <https://www.brookfieldengineering.com/learning-center/learn-about-viscosity/what-is-viscosity>.

39. Liu M, Liang L, Sun W. Estimation of in vivo mechanical properties of the aortic wall: A multi-resolution direct search approach. *J Mech Behav Biomed Mater.* 2017, Vol. 77, pp. 649-659.
40. Alimohammadi M, Sherwood JM, Karimpour M, Agu O, Balabani S, Díaz-Zuccarini V. Aortic dissection simulation models for clinical support: fluid-structure interaction vs. rigid wall models. *Biomed Eng Online.* 2015, Vol. 14, 34.
41. S. Ben Ahmed, D. Dillon-Murphy, C.A. Figueroa. Computational Study of Anatomical Risk Factors in Idealized Models of Type B Aortic Dissection. *European Journal of Vascular and Endovascular Surgery.* 2016, Vol. 52, 6, pp. 736-745.
42. SimVascular Development Team. Calculating RCR Boundary Conditions. [Online] 2017. https://github.com/SimVascular/SimVascular/wiki/user_FAQ_calculating_RCR_boundary_condition.
43. Perrin D, Badel P, Orgeas L, Geindreau C, du Roscoat SR, Albertini JN, Avril S. Patient-specific simulation of endovascular repair surgery with tortuous aneurysms requiring flexible stent-grafts. *J Mech Behav Biomed Mater.* 2016, Vol. 63, pp. 86-99.
44. David Perrin, PierreBadel, Laurent Orgéas, Christian Geindreau, Aurélien Dumenil, Jean-Noël Albertini, Stéphane Avril. Patient-specific numericalsimulationofstent-graft deployment: Validation on three clinical cases. *Journal ofBiomechanics.* 2015, Vol. 48, pp. 1868–1875.
45. David Perrin, Nicolas Demanget, Pierre Badel, Stéphane Avril, Laurent Orgéas, Christian Geindreau and Jean-Noël Albertini. Deployment of stent grafts in curved aneurysmal arteries: toward a predictive numerical tool. *Int. J. Numer. Meth. Biomed. Engng.* 2015, Vol. 31.
46. Eduardo Soudah, E. Y. K. Ng, T. H. Loong, Maurizio Bordone, Uei Pua, and Sriram Narayanan. CFD Modelling of Abdominal Aortic Aneurysm on

Hemodynamic Loads Using a Realistic Geometry with CT. *Computational and Mathematical Methods in Medicine*. 2013, Vol. 2013, 472564.

47. Tasso P, Raptis A, Matsagkas M, et al. Abdominal Aortic Aneurysm Endovascular Repair: Profiling Postimplantation Morphometry and Hemodynamics With Image-Based Computational Fluid Dynamics. *J Biomech Eng*. 2018, Vol. 140, 11, pp. 111003-111003-12.

48. Ullery, Brant W. et al. Comparative geometric analysis of renal artery anatomy before and after fenestrated or snorkel/chimney endovascular aneurysm repair. *Journal of Vascular Surgery*. Vol. 63, 4, pp. 922 - 929.

49. Sun Z, Chaichana T. Fenestrated stent graft repair of abdominal aortic aneurysm: hemodynamic analysis of the effect of fenestrated stents on the renal arteries. *Korean J Radiol*. 2009, Vol. 11, 1, pp. 95-106.

50. Wang G, Zhai S, Li T, et al. Limb graft occlusion following endovascular aortic repair: Incidence, causes, treatment and prevention in a study cohort. *Exp Ther Med*. 2017, Vol. 14, 2, pp. 1763-1768.

51. Doyle, Matthew G., Sean A. Crawford, Elrasheed Osman, Naomi Eisenberg, Leonard W. Tse, Cristina H. Amon, and Thomas L. Forbes. Analysis of Iliac Artery Geometric Properties in Fenestrated Aortic Stent Graft Rotation. *Vascular and Endovascular Surgery*. 2018, Vol. 52, 3, pp. 188-94.

52. Eberth, John, et al. Importance of pulsatility in hypertensive carotid artery growth and remodeling. *Journal of Hypertension*. 2009, Vol. 27, 10, pp. 2010-2021.

53. John F. Eberth, Natasa Popovic, Vincent C. Gresham, Emily Wilson, and Jay D. Humphrey. Time course of carotid artery growth and remodeling in response to altered pulsatility. *American Journal of Physiology-Heart and Circulatory Physiology*. 2010, Vol. 299, 6, pp. H1875-H1883 .

54. B.A. Howell, T. Kim, A. Cheer, H. Dwyer, D. Saloner, T.A.M. Chuter. Computational fluid dynamics within bifurcated abdominal aortic stent-grafts. *Journal of Endovascular Therapy*. 2007, Vol. 14, 2, pp. 138-143.

55. C.A. Figueroa, C.A. Taylor, V. Yeh, A.J. Chiou, M.L. Gorrepati, C.K. Zarins. Preliminary 3D computational analysis of the relationship between aortic displacement force and direction of endograft movement. *Journal of Vascular Surgery*. 2010, Vol. 51, 6, pp. 1488-1497.
56. C.A. Figueroa, C.A. Taylor, V. Yeh, A.J. Chiou, C.K. Zarins. Effect of curvature on displacement forces acting on aortic endografts: a 3-dimensional computational analysis. *Journal of Endovascular Therapy*. 2009, Vol. 16, 3, p. 284.
57. Idit Avrahami, Moshe Brand, Tomer Meirson, Zehava Ovadia-Blechman, Moshe Halak. Hemodynamic and mechanical aspects of fenestrated endografts for treatment of Abdominal Aortic Aneurysm. *European Journal of Mechanics - B/Fluids*. 2012, Vol. 35, pp. 85-91.
58. Jie Chen, Xi-Yun Lu. Numerical investigation of the non-Newtonian pulsatile blood flow in a bifurcation model with a non-planar branch. *J Biomech*. 2006, Vol. 39, 5, pp. 818-832.